Structural Insights on Microwave-Synthesized Antimony-Doped Germanium Nanocrystals

Katayoon Tabatabaei[a], Heather R. Sully[b], Zheng Ju[a], Kaitlin Hellier[c], Haipeng Lu[d], Christopher J. Perez[a], Kathryn A. Newton[a], Richard L. Brutchey[d], Frank Bridges*[,c], Sue A. Carter*[,c], and Susan M. Kauzlarich*[, a]

[a]Department of Chemistry, University of California, Davis, One Shields Ave., Davis, CA 95616, USA

[b]Department of Electrical Engineering, University of California, Santa Cruz, CA 95064, USA

[c]Department of Physics, University of California, Santa Cruz, CA 95064, USA

[d]Department of Chemistry, University of Southern California, Los Angeles, CA 90089, USA

*Corresponding authors: bridges@ucsc.edu, sacarter@ucsc.edu, smkauzlarich@ucdavis.edu

Abstract

Doped and alloyed germanium nanocrystals (Ge NCs) are potential candidates for a variety of applications such as photovoltaics and near IR detectors. Recently, Bismuth (Bi) as an *n*-type group 15 element was shown to be successfully and kinetically doped into Ge NCs through a microwave-assisted solution-based synthesis, although Bi is thermodynamically insoluble in bulk crystalline Ge. To expand the composition manipulation of Ge NCs, another more common *n*-type group 15 element for semiconductors, antimony (Sb), is investigated. Oleylamine (OAm)- and OAm/trioctylphosphine (TOP)-capped Sb-doped Ge NCs have been synthesized by the microwave-assisted solution reaction of GeI_2 with SbI_3. Passivating the Ge surface with a binary ligand system of OAm/TOP results in formation of consistently larger NCs compared to OAm alone. The TOP coordination on the Ge surface is confirmed by ^{31}P NMR and SEM-EDS. The lattice parameter of Ge NCs increases with increasing Sb concentration (0.00-2.0 mol %), consistent with incorporation of Sb. An increase in the NC diameter with higher content of SbI_3 in the reaction is shown by TEM. XPS and EDS confirm the presence of Sb before and after removing surface ligands with hydrazine and recapping the Ge NC surface with dodecanethiol (DDT). EXAFS analysis suggests that Sb resides within the NCs on highly distorted sites next to a Ge vacancy as well as on the crystallite surface. High Urbach energies obtained from Photothermal Deflection Spectroscopy (PDS) of the films prepared from pristine Ge NC and Sb-doped Ge NCs indicate high levels of disorder, in agreement with EXAFS data. Electrical measurements on TiO_2-NC electron- and hole-only devices show an increase in hole conduction, suggesting that the Sb-

vacancy defects are behaving as a *p*-type dopant in the Ge NCs, consistent with the vacancy model derived from the EXAFS results.

Keywords: Sb-doped Germanium, *p*-type dopant, EXAFS, XPS, Urbach energies, films, Ge nanocrystal devices

Introduction

Investigation of Group 14 semiconducting nanomaterials has increased significantly in the last few decades due to their promising properties in a broad range of technological applications.[1–4] Ge in nanoscale form is attracting tremendous research interest as bulk Ge has a suitable and narrow bulk band gap of 0.67 eV at room temperature and carrier mobilities from ~2000 (μ_h) to ~4000 (μ_e) cm^{-2} V^{-1} S^{-1}.[5] Its large exciton Bohr radius of ~24 nm[6] along with a high absorption coefficient of $\sim 2 \times 10^5$ cm^{-1} provides motivation for research towards its application in photodetectors,[7] solar energy conversion,[3,8] lithium ion batteries,[9] optoelectronics[5,10–12] and biomedicine.[13]

In addition to the ability to tune the optoelectronic properties of Ge nanocrystals (NCs) by size and shape control strategies, composition manipulation by incorporating impurities (dopant atoms) is of paramount importance, but is less explored due to challenges in synthesis.[14,15] Due to the small size of the host lattice atoms and the dramatic band structure alteration by incorporating even a small number of foreign atoms,[16] manipulating the compositions of Ge NCs enables photovoltaic, microelectronic and integrated optoelectronic applications.[17–23] The effort to produce direct band gap Ge NCs through changing their composition has been a challenge for many research groups; the efforts to tune and optimize the composition of $Ge_{1-x}Sn_x$ alloys are noteworthy examples.[8,24] Ruddy *et al.* reported the incorporation of several main group elements (E = Sn, Sb, Si, Al, P, In and Ga) in small quantities (~1 mol %) in Ge NCs by a mixed valence reduction method using n-butyl lithium as a reducing agent in octadecene to obtain $Ge_{1-x}E_x$.[23] In the nano-regime and under

kinetic control, different miscibility properties relative to their bulk can be achieved.[8,25–29] Recently, we showed the successful doping of Bi into Ge NCs using BiI_3 as a precursor.[30] Successful kinetic incorporation of Bi in Ge NCs[30,31] along with a previous report by Ruddy *et al.* showing the incorporation of Sb[23] into Ge NCs with no change in electrical transport compared to pristine Ge NC films motivated exploration of Sb as an *n*-type donor for the Ge NCs system.

Solution-based synthesis is a successful and cost-effective strategy to prepare a broad variety of nanomaterials including nano-sized Group 14 semiconductors. It can produce highly crystalline Ge NCs with well-defined size and morphology characteristics.[32,33] Among a diverse range of colloidal chemical routes to prepare Ge NCs, reduction of germanium halides is a robust and promising method to produce size-tuned Ge NCs using a mild reducing agent, such as oleylamine (OAm), as a primary alkylamine. The efficient and reproducible microwave-assisted synthesis of Ge and Bi-doped Ge NCs using the multivalent reduction of GeI_2/GeI_4 pathway was reported previously by our group.[34]

Herein, the solution-based microwave-assisted synthesis and characterization of Sb-doped Ge NCs is presented. Pristine and Sb-doped Ge NCs with three different surface ligands were investigated: OAm, OAm/trioctylphosphine (TOP) mixed ligands and 1-dodecanethiol (DDT). The mixed OAm/TOP ligands provide larger crystallite size, and ligand exchange allows for characterization of Sb incorporated into the NC by removing any physisorbed Sb at the surface. Pristine and Sb-doped Ge NCs are characterized by powder X-ray diffraction (PXRD), transmission electron microscopy (TEM), scanning transmission electron microscopy (STEM), scanning electron microscopy-energy-dispersive X-ray spectroscopy (SEM-EDS), X-ray photoelectron spectroscopy (XPS), extended X-ray absorption fine structure (EXAFS), Fourier-transform infrared spectroscopy (FTIR), nuclear magnetic resonance spectroscopy (^{1}H and ^{31}P

NMR), and photothermal deflection spectroscopy (PDS). Both electron-only and hole-only devices were prepared to probe whether the Sb serves as an active dopant.

Results and Discussion

The air-free and microwave heating-assisted synthesis of pristine and Sb-doped Ge NCs by reduction of GeI_2 using OAm as the mild reducing agent, solvent, and coordinating ligand are similar to previously reported protocols.[30,34,35] OAm, a non-polar organic primary alkylamine, commonly employed in the synthesis of a broad variety of nanomaterials due to its high boiling point, can reduce both GeI_2 and SbI_3 precursors without additional strong reducing agents.[36–38] Initially, a lower reaction temperature of 210 °C, previously reported in the literature, was chosen to prepare both pristine and Sb-doped Ge NCs. However, considering the increased crystallinity and improved stability of colloidal Ge NCs at ambient conditions, a reaction temperature of 250 °C was used to synthesize the NCs samples presented herein.[34,39,40] The reactions were heated by microwaves for a duration of 60 min, since a heating time shorter than 30 min results in incomplete growth and very small NCs. We have shown that OAm does not absorb microwave energy efficiently.[41] Hence, the Ge halides and dopant halide precursors facilitate the absorption of microwaves and allow the reaction to reach the set temperature.

To prepare Sb-doped Ge NCs, SbI_3 was utilized as the Sb source. Another Sb halide source, $SbCl_3$, has been previously shown to be reduced to elemental Sb using sodium borohydride ($NaBH_4$) and OAm.[42,43] The standard reduction potential of Sb(III) is +0.152 V, which is lower than that of Ge(II) at +0.24 V. We found that OAm by itself could reduce the SbI_3 at either at 210 °C or 250 °C in the microwave reactor.

OAm-capped Sb-doped Ge NCs. The PXRD patterns of OAm- and subsequent DDT-capped pristine and Sb-doped Ge NCs, synthesized using SbI_3 concentrations of 0 – 3.0 mol % Sb and microwave heating at 250 °C for 60 min, are shown in Figure 1(a-c). All patterns confirm the phase pure diamond cubic Ge NCs with no Sb phase segregation detected. A trend of narrowing the diffraction peaks with increasing crystallite size, attributed to increasing SbI_3 content during synthesis, is observed. Ligand exchange of OAm-capped Sb-doped Ge NCs was carried out according to a hydrazine treatment prior to recapping the surfaces with DDT.[35] The PXRD patterns of DDT-capped Sb-doped Ge NCs are shown in Figure 1(c) and their corresponding crystallite sizes are provided in Table 1. Figure 1(d) shows the lattice parameters obtained from Rietveld refinement of the OAm-capped Sb-doped Ge NCs increase from 5.6587(5) Å for pristine Ge NCs to 5.6637(3) Å for 2 mol % Sb-doped Ge NCs. Fits of PXRD with Si standard and refinement values are provided in Supporting Information (SI), Figure S1. The size of the standard deviation in the refinements, especially in the pristine Ge, arises from the broadness of the peaks due to the small particle size. Refinement of pristine Ge NCs PXRD gives rise to a lattice parameter in reasonable agreement with the bulk Ge value (5.658 Å). Lattice parameters for Ge NCs as a function of size have not been reported; as Sb is added, the lattice parameters increase, consistent with expectations for the size of the dopant and incorporation into the lattice.[44] Because the NC size also increases with Sb, if there was no incorporation of Sb into the structure, one would not expect to see the lattice parameters increase. The summary of crystallite sizes is provided in Table 1.

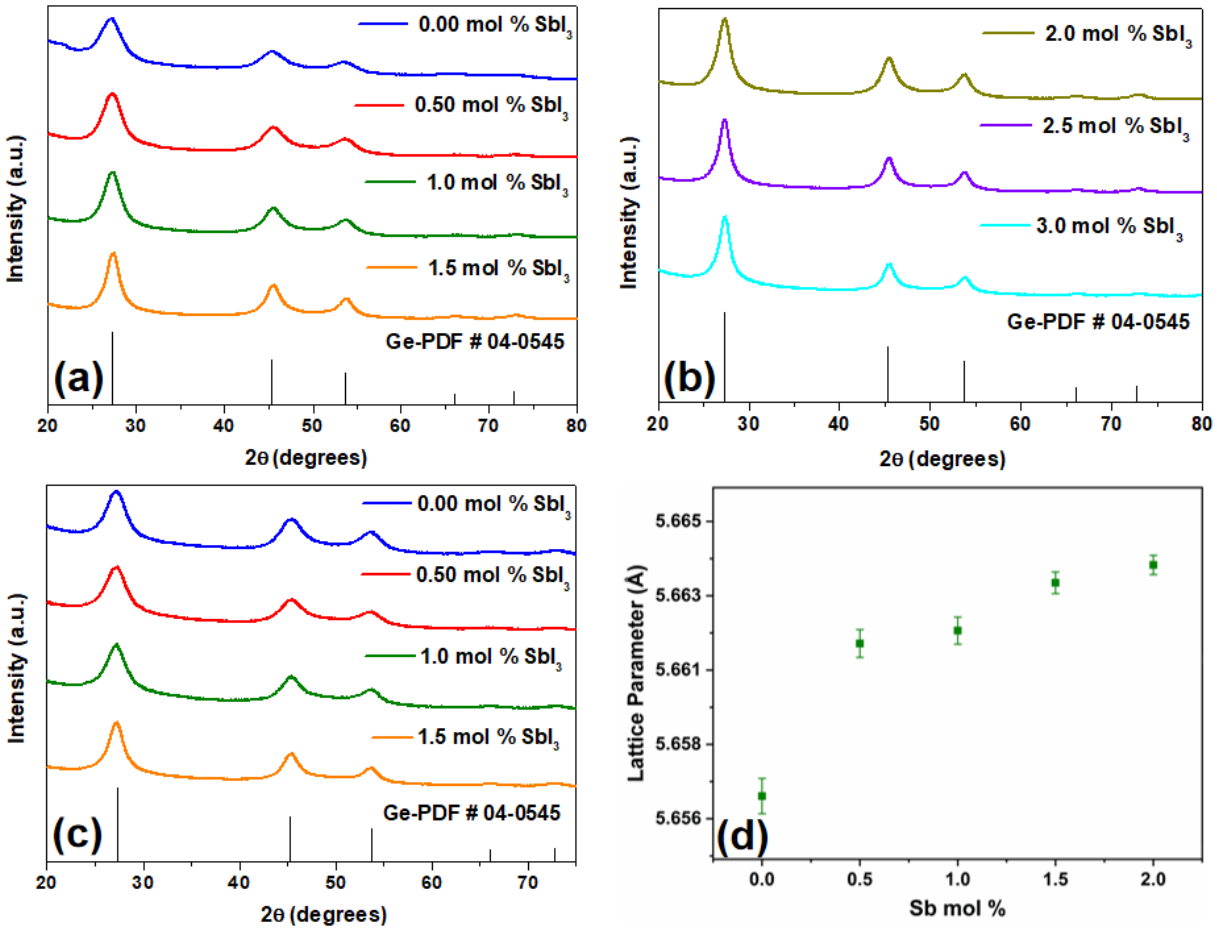

Figure 1. (a) and (b) PXRD patterns of OAm-capped Ge NCs prepared using 0.40 mmol GeI_2 with 0–3.0 mol % SbI_3 at 250 °C compared to the Ge reference pattern (PDF#04-0545). (c) PXRD patterns of DDT-capped Sb-doped Ge NCs prepared with 0–1.5 mol % SbI_3 compared to the reference pattern (PDF#04-0545). Crystallite sizes corresponding to each specific reaction temperature are provided in Table 1. (d) The lattice parameter *vs*. Sb content (0–2.0 mol %) for OAm-capped Sb-doped Ge NCs obtained from Rietveld refinement of PXRD patterns provided in Figure S1.

Table 1. Summary of Crystallite Sizes for OAm- and DDT-capped Ge NCs Obtained from Reactions with Constant 0.40 mmol GeI_2 Precursor and Increasing Amounts of SbI_3 (0–3.0 mol %) in OAm at 250 ˚C.

SbI_3 mol % (mmol)	**Crystallite Size (nm)**[‡]	
	OAm	DDT
0.00 (0.00)	3.0 ± 0.1	3.2 ± 0.1
0.5 (0.002)	3.1 ± 0.1	3.1 ± 0.1
1.0 (0.0040)	3.5 ± 0.1	3.6 ± 0.1
1.5 (0.0060)	4.4 ± 0.1	4.2 ± 0.1
2.0 (0.0080)	4.8 ± 0.1	N.D.
2.5 (0.010)	5.7 ± 0.1	N.D.
3.0 (0.012)	5.9 ± 0.1	N.D.

‡ Based on the Scherrer method employing the (220) reflection.

Figure 2 shows the representative dark field TEM images of DDT-capped pristine and Sb-doped Ge NCs synthesized with different amounts (0 – 1.5 mol %) of SbI_3. The TEM image of pristine Ge NCs shows quasi-spherical particles with an average diameter of 5.9 ± 0.62 nm with no evidence of agglomeration. The larger diameter obtained from TEM compared with the crystallite size from powder diffraction is consistent with polycrystalline particles. An increase in Ge NC diameters from 5.9 ± 0.62 nm to 7.4 ± 1.3 nm with higher SbI_3 concentrations is observed. Besides the observed increase in particle sizes, a broader size distribution with higher concentrations of dopant precursor is also detected. Similar trends were also obtained using BiI_3 as the *n*-type dopant precursor for Ge.[30] The impairment of growth kinetics, which is attributed to the interaction of dopant and host, and their contribution to the chemical potentials and surface energies in the nano-regime, is still a challenge to be addressed in composition manipulation of NCs. Using higher SbI_3 concentrations, in particular 3.0 and 5.0 mol %, result in aggregation of Ge NCs and unstable NC dispersions. A similar interaction with dopant precursors has been shown

for CdSe NCs in the presence of $InCl_3$, to disrupt the growth kinetics of host seeds and resulting in a broad size distribution.[45]

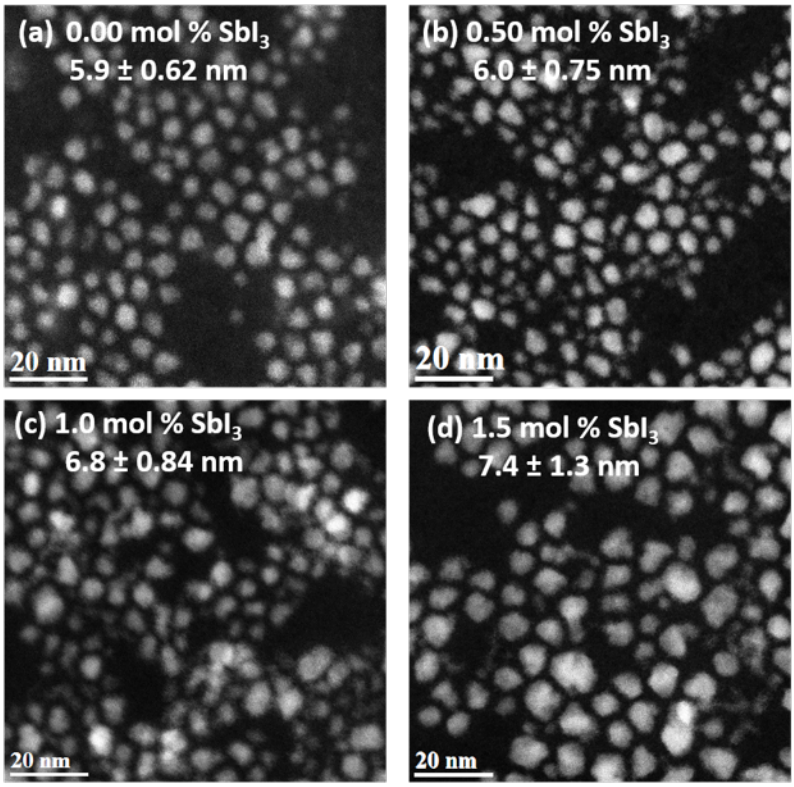

Figure 2. Representative dark field STEM images of DDT-capped Sb-doped Ge NCs (0 – 1.5 mol % SbI_3) after OAm ligand exchange. At the top of each image, the quantity of dopant precursor, average diameter and size distribution are provided. Size distribution and corresponding histograms for each sample are shown in Figure S4. Higher anisotropy of particle morphology is observed in Ge NCs prepared with higher SbI_3 concentrations, implying the loss of growth kinetics as discussed previously.

OAm/TOP-capped Sb-doped Ge NCs. TOP was employed with OAm because the chemical nature and physical dimension of surface ligands can influence the nucleation and growth kinetics of NCs.[46–48] TOP has been shown to affect the growth mechanism of NCs,[49] particularly when applied as a co-surfactant and coordinating solvent to prepare metal chalcogenide nanomaterials.[50] For all the following reactions, a consistent quantity of TOP (1.0 mL) with 7.0 mL OAm was employed in the reaction mixture. The PXRD patterns of the OAm/TOP-capped and their corresponding DDT-capped Ge NCs are provided in Figure S3. The crystallite sizes of OAm/TOP- and DDT-capped pristine and Sb-doped Ge NCs are summarized in Table 2. Similar to above, the DDT-capped are about the same size as the OAm/TOP-capped. There is a consistent increase in crystallite sizes for the OAm/TOP- and corresponding DDT-capped**,** compared to using OAm only (Table 1) as the surface ligand. Hence, TOP can be used to control the Ge NCs sizes as another size control strategy. No other phase corresponding to Sb phase segregation was observed.

Table 2. Crystallite Sizes for OAm/TOP and DDT-capped Ge NCs Obtained from Reactions with Constant 0.40 mmol GeI_2 Precursor and Increasing Amounts of SbI_3 (0-1.5 mol %) in OAm at 250 ˚C

SbI_3 mol % (mmol)	**Crystallite Size (nm)**‡	
	OAm/TOP	DDT
0.00 (0.00)	3.5 ± 0.1	3.6 ± 0.1
0.500 (0.002)	4.2 ± 0.1	4.1 ± 0.1
1.0000 (0.0040)	5.0 ± 0.1	5.4 ± 0.1
1.5000 (0.0060)	7.1 ± 0.1	6.8 ± 0.1

‡ Based on the Scherrer method employing the (220) reflection.

The corresponding bright and dark field STEM images of OAm/TOP-capped Sb-doped Ge NCs (prepared with 0.00-1.5 mol % SbI_3) are presented in Figure 3 and in SI, Figure S4, respectively. In agreement with images using only OAm as a coordinating ligand, an increase in particle diameter is observed by using higher SbI_3 concentrations from 0 to 1.5 mol%. In addition, the loss of growth kinetics and the higher degree of morphology irregularity seem to be inevitable even with having TOP along with OAm as the surface ligand. At 1.5 mol % SbI_3, agglomerated Ge NCs result, providing a broad size distribution. A high-resolution STEM image (HR-STEM) of Sb-doped Ge NCs with 1.5 mol % SbI_3 is shown as an inset in Figure 3(d). It provides single crystal lattice fringes characteristic of the diamond cubic Ge. The histograms of Ge NC diameters and their fit to a Gaussian model are provided in Figure S5.

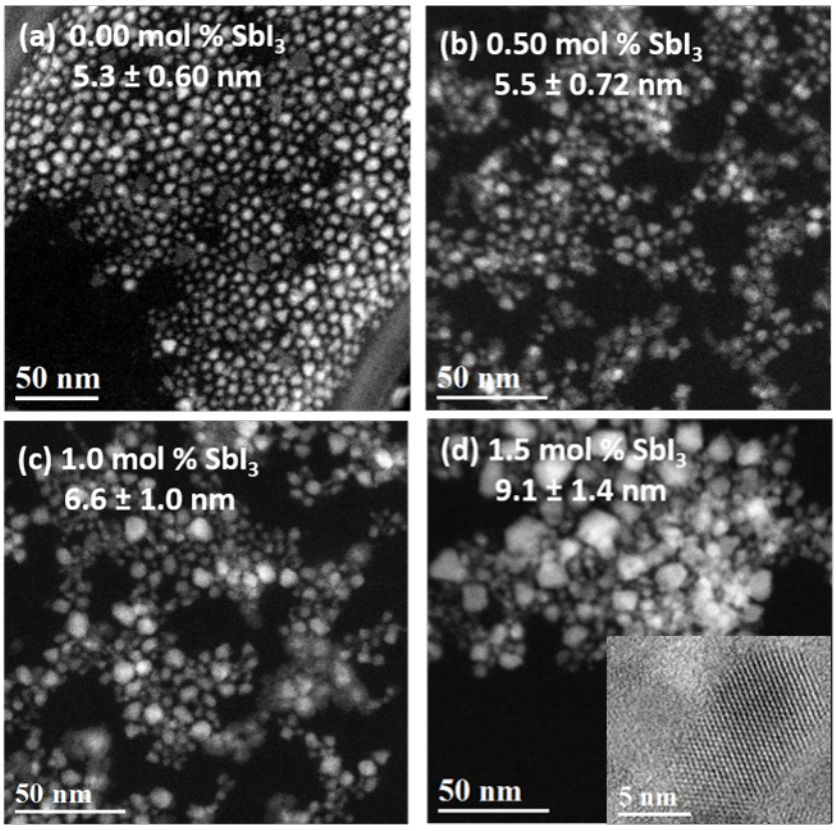

Figure 3. Representative dark field TEM images of OAm/TOP-capped pristine and Sb-doped Ge NCs with 0.40 mmol GeI_2 and varying amounts of SbI_3 (0-1.5 mol%). At the top of each image, the quantity of dopant precursor, average diameter and size distribution are provided. The inset in (d) shows the high-resolution bright field STEM (HRSTEM) image with clear lattice fringes for 1.5 mol% Sb-doped NCs. The bright field TEM images and corresponding histograms are shown in SI, Figures S4-S5.

Surface Characterization. The surface chemistry of Sb-doped Ge NCs capped with OAm/TOP *versus* DDT were studied by FTIR and the corresponding absorbance spectra are shown in Figure 4. The FTIR transmission spectra of OAm and the corresponding DDT-capped Sb-doped Ge NCs are provided in Figure S6, for 1.5 mol % Sb-doped Ge NCs as a representative sample. The absence of the characteristic alkenyl C-H stretching vibration at ~3005 cm^{-1} in the DDT-capped Ge NC FTIR spectrum indicates the complete removal of OAm ligands through hydrazine treatment and recapping the surface with DDT.

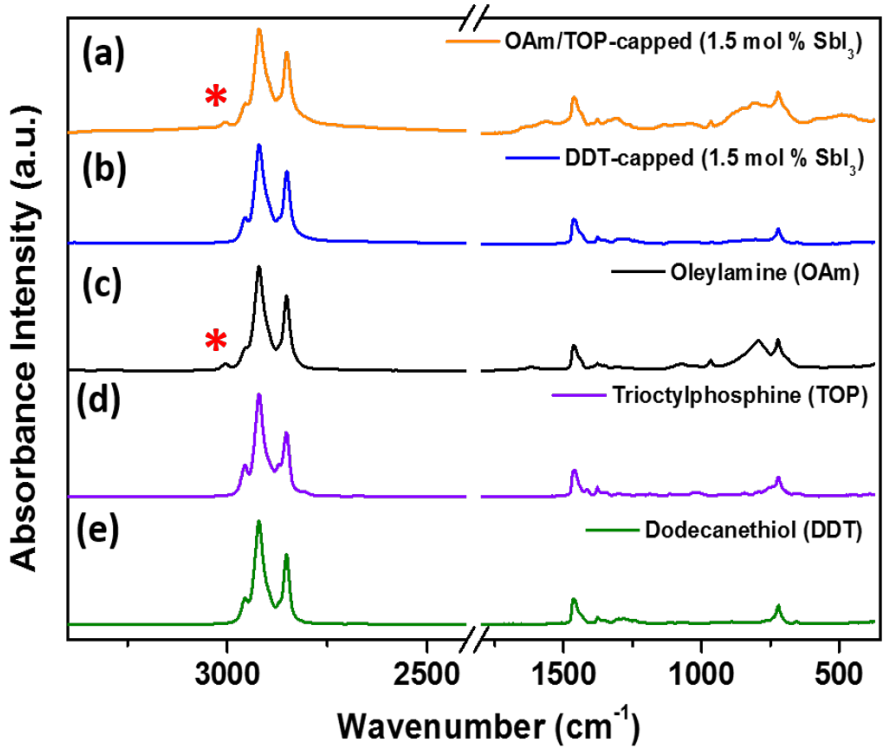

Figure 4. FTIR absorbance spectra of (a) OAm/TOP- and (b) DDT-capped Ge NCs from the reaction with 1.50 mol % SbI_3. The spectra of pure solvents as references are shown in (c) OAm, (d) TOP and (e) DDT. The red asterisk on spectra (a) and (c) shows the alkenyl C-H stretching vibration at ~3005 cm^{-1}. The spectra in transmittance mode are provided in Figure S7.

^{1}H and ^{31}P NMR were performed on OAm/TOP and DDT-capped Sb-doped Ge NCs (Figures 5, 6). The absence of a vinylic proton peak between 5 and 6 ppm indicates the complete removal of OAm ligands through hydrazine treatment.[35,51] Recently, we reported a detailed solution NMR study on OAm-capped Ge NCs synthesized at different temperatures to determine the binding mode of this native primary amine on the Ge surface.[52] Two distinct fractions of both weakly physisorbed and strongly covalent X-type bonded OAm on the Ge surface were resolved by exchange reactions with different functional groups (amines/ammonium, thiols and carboxylic acids). It was shown that their fraction ratio directly correlates with the reaction temperature.[52] The broadening of NMR peaks and the chemical shifts slightly downfield compared to unbounded ligands are characteristic for nanomaterials.[53,54] The ^{31}P NMR signal at −32.2 ppm compared to −30.6 ppm of free TOP confirms the binding of TOP on the Ge NCs surface. The peak at −56.6 ppm in ^{31}P NMR can be attributed to trioctylphosphine oxide (TOPO) upon oxidation of the sample. Following DDT ligand exchange, no ^{31}P NMR signals attributed to the ligands were detected, suggesting the complete removal of TOP from the surface of Ge NCs through hydrazine treatment. (Figure S8)

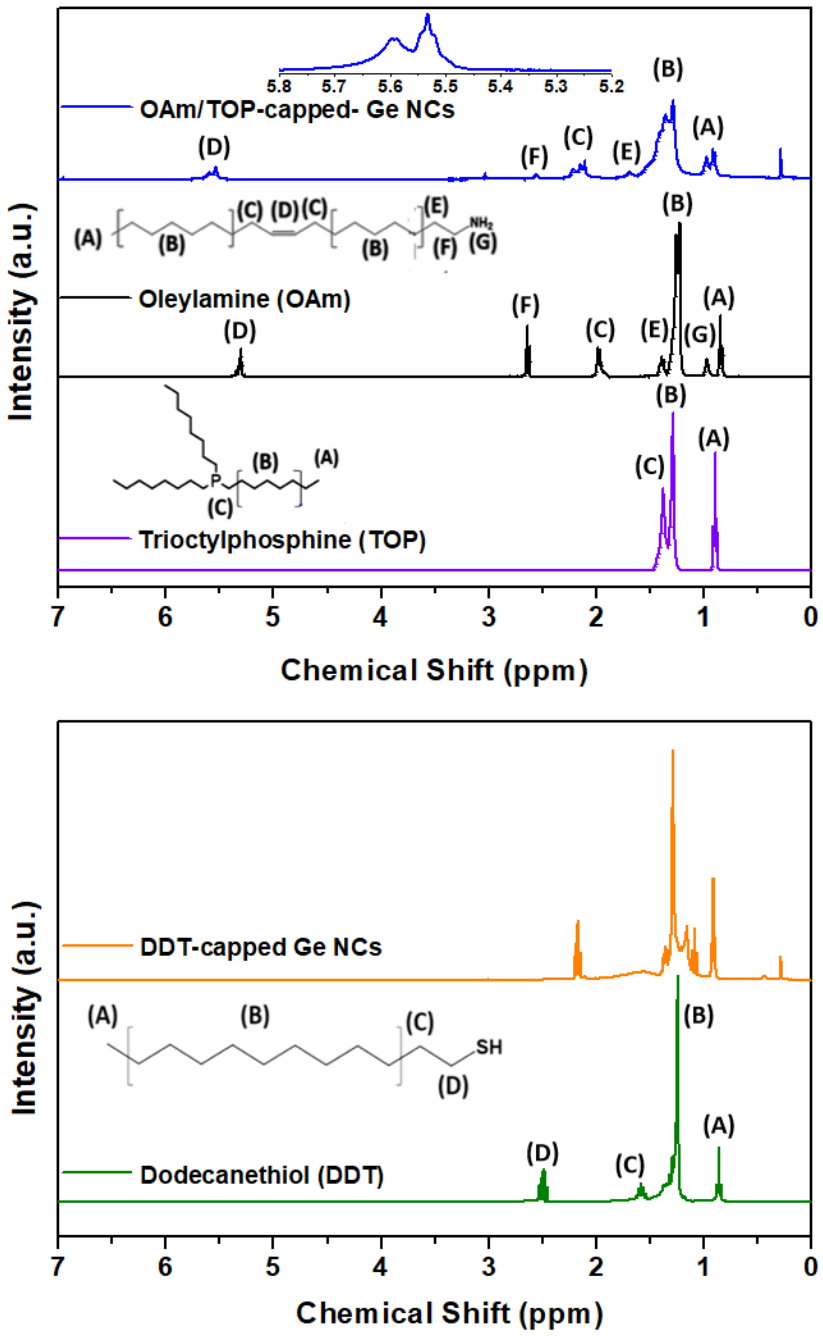

Figure 5. (a)[1]H NMR spectrum for OAm/TOP-capped Sb-doped Ge NCs. The vinylic proton region (peak D) is expanded in the top spectrum. The spectra of OAm and TOP are also shown. (b) [1]H NMR spectrum for DDT-capped Sb-doped Ge NCs. The spectrum of DDT is also shown.

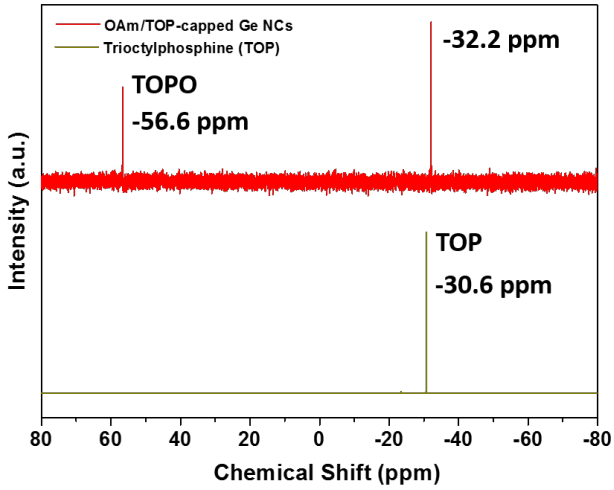

Figure 6. ^{31}P NMR spectrum for OAm/TOP-capped Sb-doped Ge NCs (top). The spectrum of pure TOP is also provided (bottom).

Figure 7 and Figure S9 show the elemental mapping under SEM (EDS-SEM) and EDS spectroscopy of films prepared from OAm- and DDT-capped Ge NCs using 1.5 mol % SbI_3. Images of 2.0 mol % SbI_3 are provided in Figures S10 and S11. The Ge, Sb, and their overlay elemental mappings show the homogenous distribution of both elements throughout the sample area. EDS was performed to reveal the average elemental composition of the Sb-doped Ge NCs. In the EDS spectra, characteristic peaks for Ge, Sb, C, O, and Si are clearly distinguished. The silicon signal is attributed to the substrate. The oxygen signal is attributed to slight oxidation of the Ge NCs in the process of sample preparation under ambient conditions. The Sb L_α peak at 3.60 keV confirms the presence of Sb. The signal attributed to S at 2.3 keV is clearly observed for DDT-capped NCs (provided in Figures S11 and S12). The presence of the Sb signal in samples capped with DDT following removal of OAm ligands through hydrazine treatment confirms either the incorporation of Sb in the Ge NCs or strong binding of Sb atoms to the Ge surface. The relative

ratio of Sb to Ge from EDS for the various films follows a consistent trend with the expected composition according to the amounts of starting reagents.

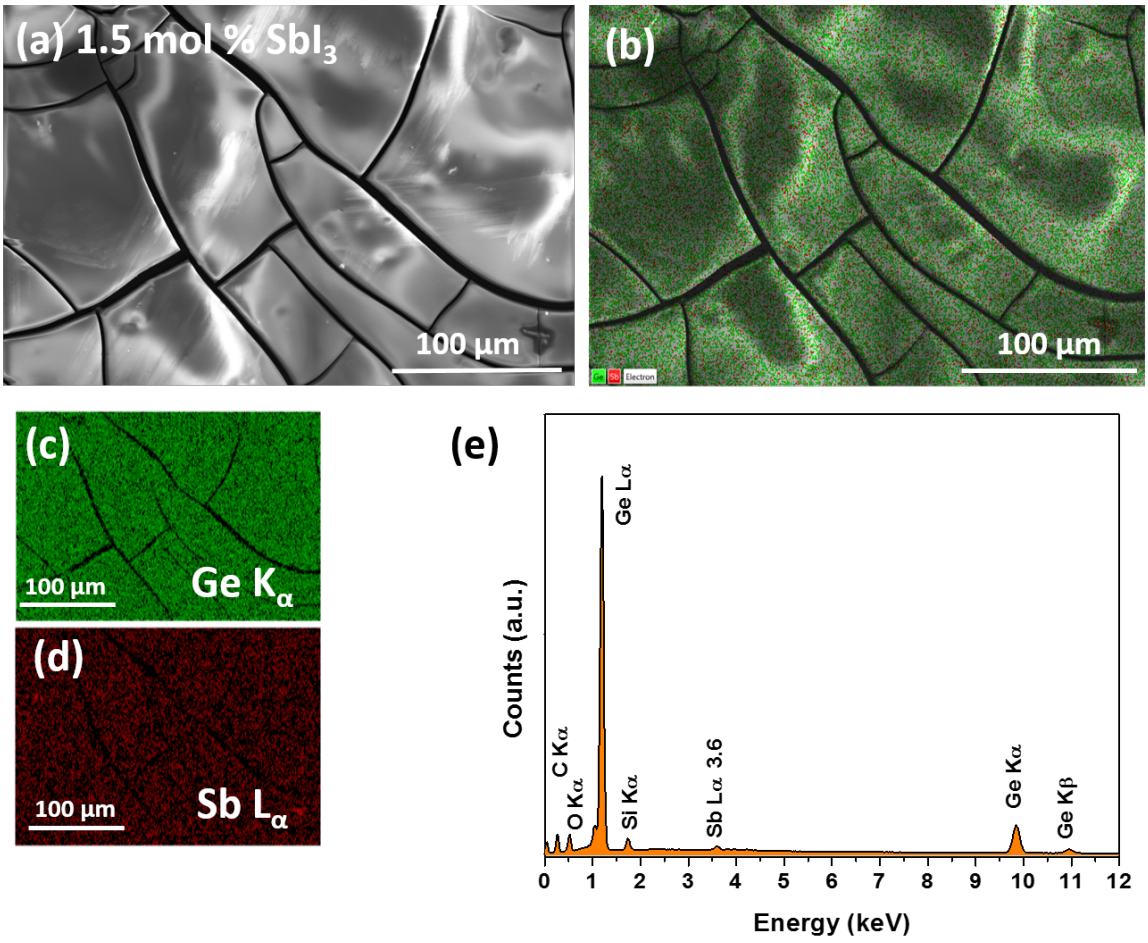

Figure 7. (a) Representative SEM image of OAm-capped Sb-doped Ge NCs prepared from the reaction with 1.5 mol% SbI_3. (b) Elemental mappings corresponding to overlay of both Ge (green) and Sb (red), and individual mappings of (c) Ge and (d) Sb. (e) EDS spectrum of the same area shown in (a).

Figure 8 and Figure S12 provides the SEM-EDS mappings and corresponding spectra of OAm/TOP and DDT-capped Sb-doped Ge NCs for 1.0 mol % Sb. Mappings and spectra for 1.5 mol% SbI_3 are shown in Figures S13 and S14. The presence of Sb L_α at 3.60 keV in all the samples

is clearly observed. A peak at 2.03 keV characteristics of P K_α confirms the presence of TOP ligands on the surface of the NCs. All samples were washed multiple times to ensure the complete removal of any unassociated organic ligands. The absence of P signal for DDT-capped NCs agrees with complete phosphine ligand displacement. The presence of Sb signals in all samples confirm the incorporation of Sb within or at the surface of Ge NCs.

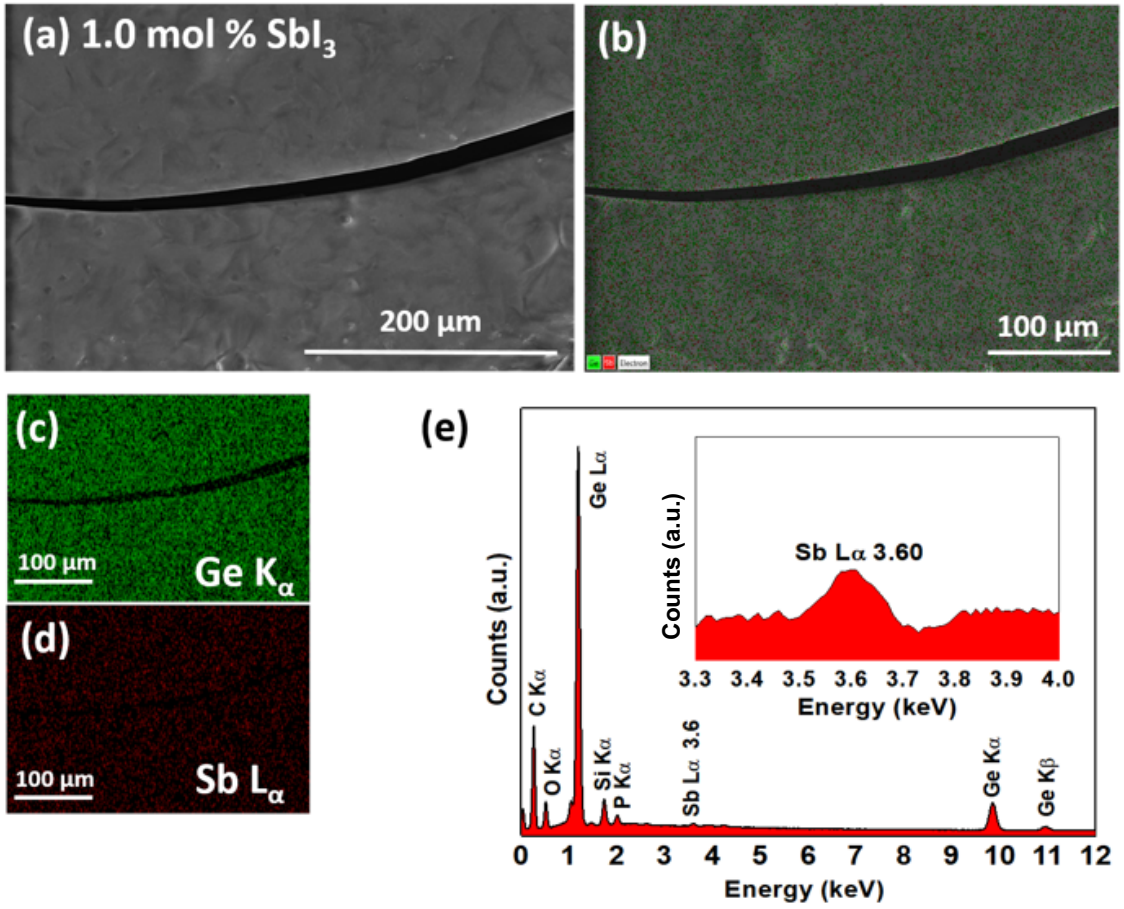

Figure 8. (a) Representative SEM image of OAm/TOP-capped Sb-doped Ge NCs using 1.0 mol % SbI_3. (b) Elemental mapping corresponding to overlay of both Ge (green) and Sb (red), and

individual mappings of (c) Ge and (d) Sb. (e) EDS spectrum of the same area shown in (a), the inset shows the expanded Sb signal areas.

XPS. High-resolution X-ray photoelectron spectroscopy (XPS) analysis of DDT-capped Sb-doped Ge NCs prepared with 1.0 mol % SbI_3 are shown in Figure 9. 2.0 mol % SbI_3 data are similar and provided in Figure S15. Characteristic Ge signals with binding energies of 1248 and 1217 eV are observed for Ge $2p_{1/2}$ and Ge $2p_{3/2}$, respectively. The S 2p peaks observed in the XPS spectra possess binding energies of ~163 eV being assigned to S 2p peak. The presence of S 2p peaks indicate the successful DDT ligand exchange of NCs upon hydrazine treatment and recapping their surfaces with thiol molecules. Sb signals with binding energies of 528 and 537 eV corresponding to Sb $3d_{5/2}$ and Sb $3d_{3/2}$, respectively, are observed in both samples.

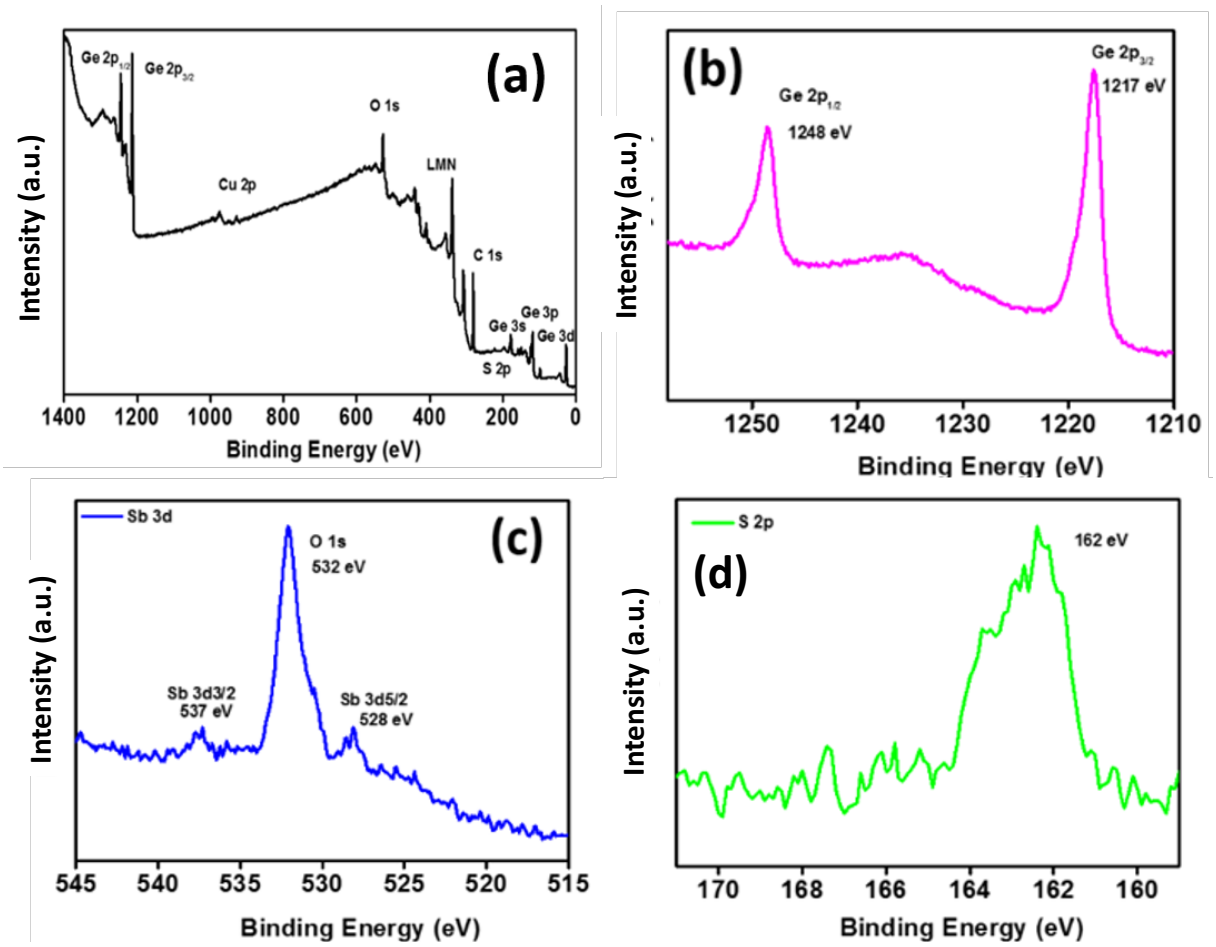

Figure 9. (a) Survey and high-resolution (b) Ge 2p, (c) Sb 3d, and (d) S 2p XPS spectra for DDT-capped Sb-doped Ge NCs prepared using 1.0 mol % SbI_3. The presence of the O 1s peak with binding energy of 532 eV is attributed to the XPS sample preparation under ambient condition.

Ge EXAFS data. The EXAFS spectra for the Ge edge are shown in Figure 10 for doped and pristine Ge NCs. In *r*-space, the real part *R* of the FFT is the fast oscillating function and provides a measure of the phase, while $\pm\sqrt{R^2 + I^2}$ (I is the imaginary part of the FFT) are the envelope functions seen in Figures 10 and 11. For the Ge K edge, the data were fit to a sum of three Ge-Ge FEFF7 functions[55] for the first, second, and third neighbors in crystalline Ge. For small NCs, the number of neighbors is expected to be smaller than in bulk because of surface effects, and these values were allowed to vary, along with distances and σ. Table 3 reports the amplitudes for pristine and

Sb-doped Ge NCs of various sizes, extracted from fits of the Ge K edge data, along with crystallite size calculated by Scherrer analysis of XRD patterns. The Ge NCs synthesized for this study are multigrain, as seen in the TEM images, meaning that the particle is made up of several crystallites. Consequently, surface induced disorder is dependent on crystallite size and surface doping includes dopants on or at the grain boundaries between crystallites, as well as on the NC surface.

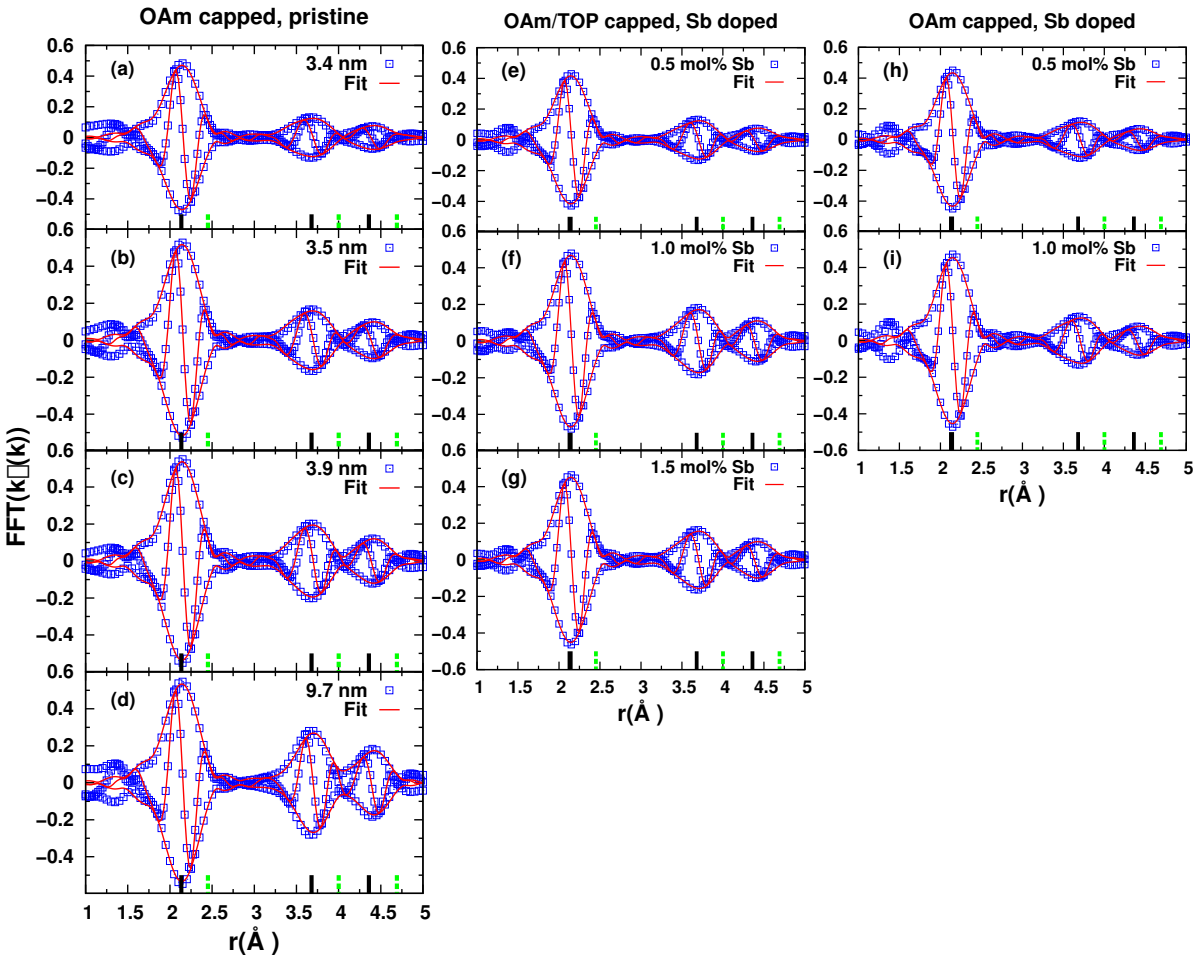

Figure 10. Ge K edge. *k*-weighted EXAFS data in r-space (points) and fits (red line) for the (a-d) pristine and (e-i) Sb-doped Ge NC samples. FT range was 3.5 to 14.5 $Å^{-1}$. Crystallite size was calculated from PXRD using Scherrer analysis. Fit results are reported in Table 3. Green (dashed) lines indicate the calculated distances from diffraction of first, second and third neighbors in bulk

Ge (Table S1). The black lines indicate the expected peak locations for these neighbors on an EXAFS spectrum for an undistorted lattice.

Table 3. Ge K Edge EXAFS Nearest Neighbors (NN) of Bulk Ge, Pristine and Sb-doped Ge NCs (OAm and OAm/TOP-capped)

Crystallite Size (nm)	SbI_3 mol %	Surface Ligand	Ge-Ge (1^{st} NN)‡	Ge-Ge (2^{nd} NN)‡	(1^{st} NN)/(2^{nd} NN)
Bulk Ge	-	-	4.0	12	0.33
3.4	0.00	OAm	3.0	6.5	0.46
3.5	0.00	OAm	3.3	6.8	0.49
3.9	0.00	OAm	3.4	7.2	0.47
9.7	0.00	OAm	3.6	8.4	0.43
3.1	0.50	OAm	2.6	4.8	0.60
4.4	1.50	OAm	2.8	5.1	0.57
4.2	0.50	OAm/TOP	2.7	4.5	0.55
5.0	1.0	OAm/TOP	3.2	5.6	0.54
7.1	1.5	OAm/TOP	3.0	5.5	0.54

‡ Errors on the number of neighbors are 15%.

Peak amplitudes in the Ge edge EXAFS data for all NCs are lower than for bulk Ge. This is expected as the high surface area of NCs exposes surface atoms to fewer neighbors. The amplitudes (number of neighbors) of the nearest neighbor peaks for doped samples are lower than for pristine NCs, but considering that the amplitude values have 15% error, the differences are not large except for the 1.5 mol % Sb sample. However, the amplitude is systematically lower for all Sb-doped samples, indicating increased disorder for the doped NCs even though diffraction results indicate

larger grain sizes for the Sb-doped samples. The second nearest neighbor values are significantly lower (~1) for doped NCs compared to pristine Ge NCs of comparable particle size, further indicating increased disorder of the Ge lattice. For comparison, the ratio of 1st to 2nd nearest neighbor amplitudes is reported in the last column of Table 3. Bulk Ge has a ratio of 0.33. Pristine Ge NCs have ratios from 0.43 to 0.49, with the largest NC sample having a ratio closest to bulk which is in agreement with a lower surface to volume ratio for larger crystals. Sb-doped NCs have higher ratios, between 0.60 to 0.54. Both the higher ratios of doped to pristine samples and the low number of second neighbors for Sb doped NCs indicate a higher amount of disorder associated with the Ge atoms for doped samples. This suggests that doping with Sb significantly increases disorder throughout the Ge lattice. The values of some σ^2 for the Ge edge are given in Table S2.

Sb EXAFS data. The Sb K edge r-space EXAFS data are shown in Figure 11 for OAm/TOP-capped and OAm-capped Sb-doped Ge NCs with varying dopant concentration (0.50, 1.0, 1.5 mol % Sb). The first peak near 2.3 Å is the nearest neighbor Sb-Ge peak, but is significantly shifted to larger *r*; compare the peak position with the black bar near 2.1 Å. Also note that the peak amplitudes are highest for the lowest Sb concentration, particularly for the further neighbor peaks, and that the amplitudes are smaller for OAm capped samples compared to the OAm/TOP capped samples.

Two models were created to fit the Sb K edge spectra. The first considers substitution within the surface layer, where large distortions are easily accommodated. Using an Sb atom on an undistorted Ge site in the Ge diamond crystal lattice, FEFF7 was used to generate theoretical EXAFS functions for Sb-Ge pairs of atoms (for first, second and third nearest neighbors). Large bond length expansions were then allowed for the nearest neighbor bond lengths to account for the large covalent (atomic) radius of Sb relative to Ge; amplitudes for the 2nd and 3rd neighbors of the

surface model were set equal. This model was a good fit for the first peak. Shifts for this peak were between 0.20 and 0.22 Å, matching well with the difference in covalent radius (0.19 Å) between Ge and Sb (Ge = 1.20 Å, Sb = 1.39 Å). The number of neighbors were between 2.2 and 2.7 matching the expected 2 to 3 neighbors for Sb atoms residing on Ge lattice surface sites. Surface sites provide an environment for the expansions required for Sb substitution and in the case of Bi-doped Ge NCs, EXAFS suggests that the Bi is located at or near the surface or interface of crystallites.[31]

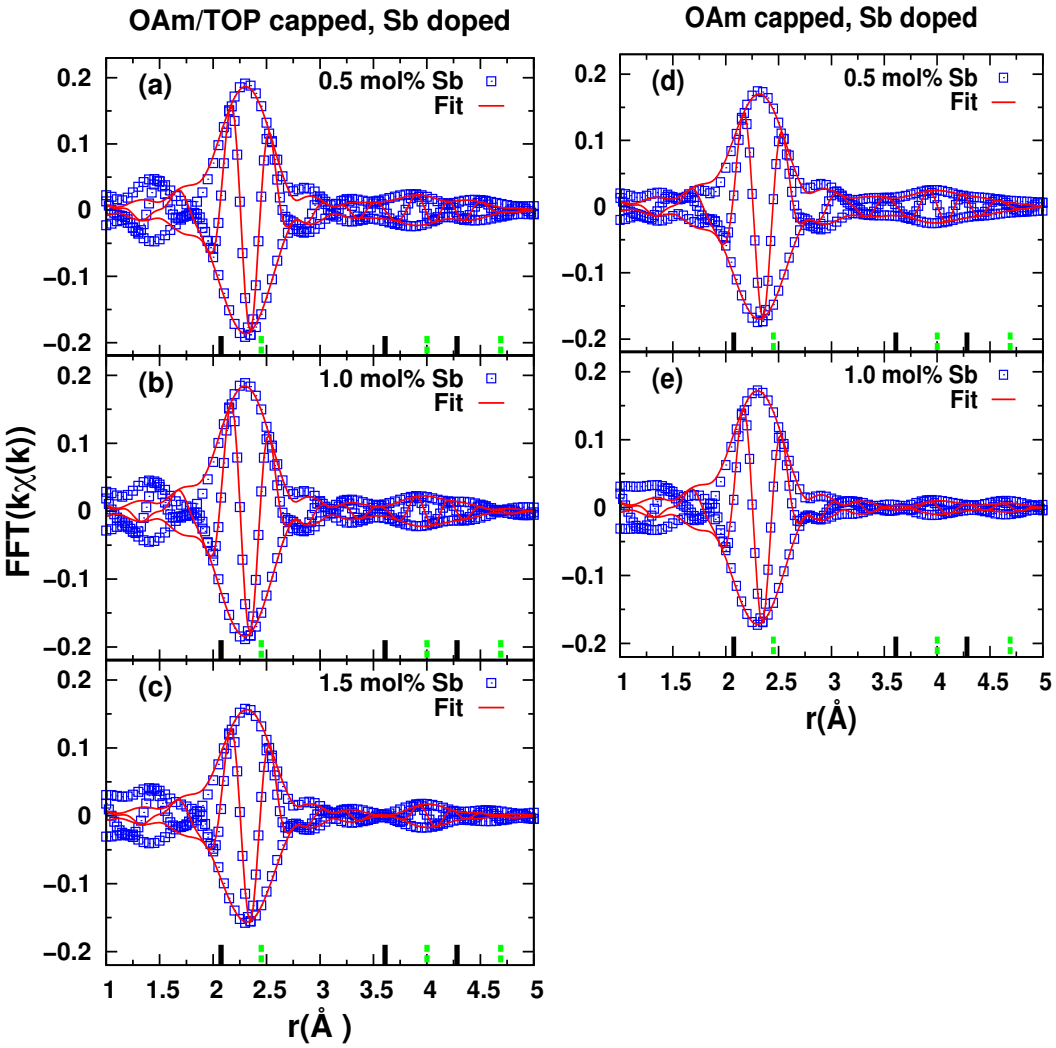

Figure 11. Sb edge EXAFS data (open squares) collected for (a-c) OAm/TOP-capped and (d and e) OAm-capped Sb-doped Ge NCs and *r*-space fits (line). The SbI_3 concentration used in each reaction is provided in the legend. FT ranges for Sb *K* edges are 4.5-13.5 $Å^{-1}$. Green dashed lines indicate the calculated distances from diffraction of first, second and third neighbors in bulk Ge. The black lines indicate the expected peak locations for these neighbors on an EXAFS spectrum for an undistorted lattice.

There were several inconsistencies with the first model that places Sb dopants only on the surface. First, the number of neighbors for the second and third peaks (Sb data) were lower than expected. An Sb atom on a surface site would have roughly half the number of second and third nearest neighbors as a bulk site (6 neighbors instead of 12). However, fits resulted in low values of further neighbors and large values for σ^2. Second, surface site occupation does not account for the small lattice expansion with doping concentration found in the PXRD results. Third, for the Ge EXAFS discussed above the number of second neighbors was smaller in the Sb doped samples (Table 3), compared to pristine Ge samples. The lower second neighbor amplitude is surprising since Scherrer analysis showed that the Sb-doped crystallites are larger, which should lead to larger second neighbor peak amplitudes. This indicates that there is a higher amount of local disorder inside the crystallite for higher Sb concentrations.

For these reasons, a model that puts some Sb atoms off-center within the crystallite of the NC was considered. This alternative model places Sb on a Ge site adjacent to a vacancy, a known type of defect found in Sb-doped Ge.[56] Distortion is accommodated by displacing the Sb atom off-center by 0.5 Å towards the vacancy and away from the three remaining Ge nearest neighbors; this gives the Sb-Ge distance for closest Ge neighbors that is observed in our data. Theoretical EXAFS

pair functions were generated for this model; Table 4 shows the resulting numbers of neighbors and the distances.

Displacing the Sb atom off-center causes further neighbor pair distances to split into three: short, medium, and long distances, with the number of neighbors at each distance given by the ratios of 3:6:3 and 6:3:3 for the original 2nd and 3rd neighbors, respectively. The amplitude of the 1st neighbor was allowed to vary. The simplified illustration in Figure 12 (a) shows the splitting on 6 of the second nearest neighbors. The red, green, and orange dotted lines are the shortened, medium, and elongated paths between Sb atom and the second nearest neighbor. Although some splitting of the second nearest neighbor distances is expected for a surface Sb atom model, the distortion is more easily accommodated at a surface site, and bond expansions at the second and third neighbors are under 0.1 Å. Figure 12(b) shows the plot of the change in the number of neighbors with increasing off-center shift of the Sb atom, assuming no other rearrangement of the neighboring Ge atoms.

Table 4. Number of Nearest Neighbors (NN) and Distances for Theoretical EXAFS Pair Functions for an Sb Atom Located 0.5 Å Off-center from a Ge Lattice Site and Next to a Vacancy

Path Function (NN)‡	Number of Neighbors	Distance (Å)
1st NN	3	2.66
2nd NN (short)	3	3.60
2nd NN (medium)	6	4.03
2nd NN (long)	3	4.42
3rd NN (short)	6	4.45
3rd NN (medium)	3	4.80
3rd NN (long)	3	5.13

‡ The second and third neighbor signals are split into short, medium and long distances

When the FEFF7 functions for peaks at different positions are summed, the real parts of these EXAFS functions interfere, causing the r-space EXAFS amplitude to be suppressed. In addition, an off-center Sb atom introduces additional disorder which pushes surrounding Ge atoms slightly off their lattice sites causing the widths of EXAFS peaks to broaden significantly.

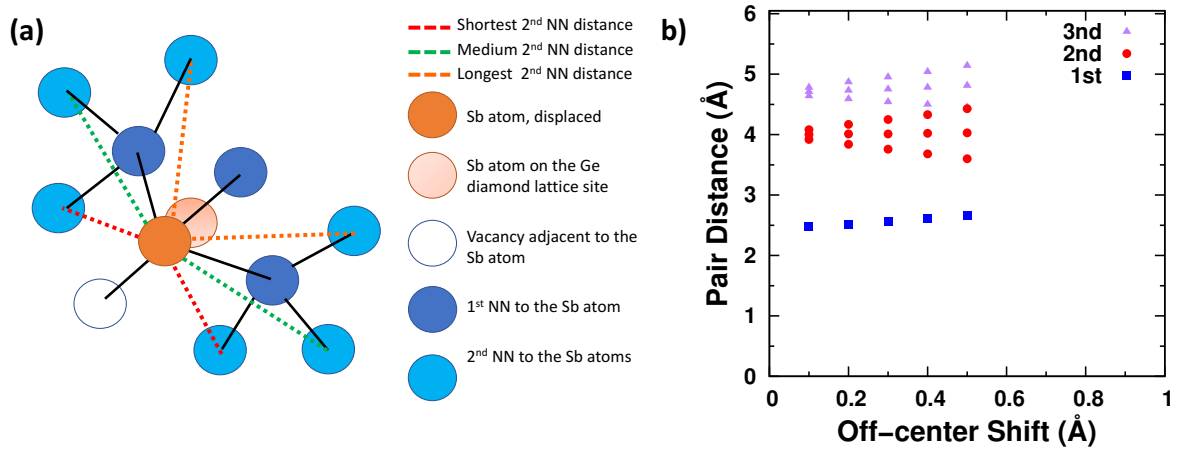

Figure 12. (a) Illustration showing the splitting of the EXAFS functions for an Sb atom located within the Ge lattice and adjacent to a vacancy, with first and second near neighbor (NN) distances indicated. (b) Plot showing the change in the pair distances for split EXAFS functions with an off-center displacement of the Sb atom.

The best fits used path functions from both models so that a mixed percentage of Sb dopants are on surface sites and within the crystal; these fits are summarized in Table 5. However, the fractions, *f*, are difficult to quantify because a peak near 4 Å, is present in both models. It arises from second neighbor bonds that are approximately perpendicular to the Sb off-center displacement direction and hence do not change much when Sb is displaced. Because there are different possible surface sites, roughly 1/3 of the amplitude of this peak comes from surface sites, and the other 2/3 comes from the Sb-vacancy pair. This peak has less broadening than other peaks

listed in Table 5 likely because it is less sensitive to Sb displacement. In the fits, the number of neighbors in each peak for the off-center Sb site are fixed to those in Table 4, and the pair distances are determined by the off-center displacement of Sb which is allowed to vary. Also, the amplitudes of the second and third neighbor from the surface model were set equal. The fraction *f,* of interior sites (1-*f* surface sites) was allowed to vary but was sensitive to changes in constraints, and hence the uncertainty is large, 20-25%. A general feature of these fits is that *f* is larger for the OAm/TOP-capped samples and decreases as the Sb concentration increases, suggesting that for the high Sb concentrations most of the Sb goes into surface sites.

The fit range is 1.9-4.8 Å and the number of parameters that were varied ranged from 11 to 13. The corresponding numbers of degrees of freedom were 7.6 to 5.6. The main constraints that were varied were for some σ's; some peaks were strongly broadened and contributed little amplitude. Fixing the value of these σ's did not change the goodness of fit parameter significantly. The values of some σ^2 for the Sb edge are given in Table S2.

Table 5. Number of Neighbors and Distances from a Fit using a Mixed Model with a Fraction (*f*) of the Sb atoms Off-center Towards a Vacancy within the NC, and a Fraction (1-*f*) on the NC Surface

path (NN)	0.50 mol % OAm/TOP	1.0 mol % OAm/TOP	1.5 mol % OAm/TOP	0.50 mol % OAm	1.0 mol % OAm
Number 1st NN (Å)	2.9(3)	2.8(4)	2.6(4)	2.8(4)	2.5(4)
1st NN distance (Å)	2.862(5)	2.855(5)	2.867(5)	2.867(5)	2.859(5)
Sb atom off-center displacement (Å)	0.49(1)	0.47(1)	0.50(1)	0.50(1)	0.49(1)
Fraction Inside (*f*)	0.83	0.52	0.13	0.63	0.08

Main 2nd NN peak Amplitude‡	5.5(5)	4.4(5)	3.1(9)	4.8(5)	3.0(9)
Main 2nd peak distance (Å)	4.07(2)	4.11(2)	4.09(3)	4.11(2)	4.12(3)

‡ For the Off-center Sb, except for the peak near 4 Å, the amplitudes were constrained to those in Table 4 and the distances determined in terms of the Sb off-center distance. The peak near 4 Å is the main second neighbor peak and has contributions from both the off-center Sb site and surface sites as described in the text.

PDS. PDS measurements were performed on 115 nm thick OAm/TOP-capped pristine and 130 nm thick 0.5 mol % Sb-doped Ge NC films, shown in Figure 14. Tauc plots, shown in the inset, give approximate band gaps of 0.90 ± 0.05 eV and 0.96 ± 0.05 eV for pristine and Sb-doped Ge NC films, respectively. Due to the nature of NCs (size dispersion, surface defects, and the smearing of the band edge), a more accurate gap is difficult to determine. OAm-capped pristine Ge NCs (Bohr exciton radius of Ge ~ 24 nm) with the particle sizes of 3.8 ± 0.8 nm, 4.3 ± 1.0 nm, and 4.6 ± 0.61 nm previously reported by Neale *et al.* and our group indicated band gaps of 1.06–1.30 eV, slightly higher than what is reported here.[4,30,34,41] The inclusion of TOP consistently increases the NC particle size compared with OAm alone, likely accounting for the smaller reported gaps. Fits were performed assuming an indirect gap, as the direct relation did not give good fits, implying that a strain-induced transition to a direct gap was not achieved. High Urbach energies of 127 ± 5 meV for the pristine Ge NC and 124 ± 5 meV for the Sb-doped Ge NC indicate high levels of disorder, in agreement with EXAFS data.

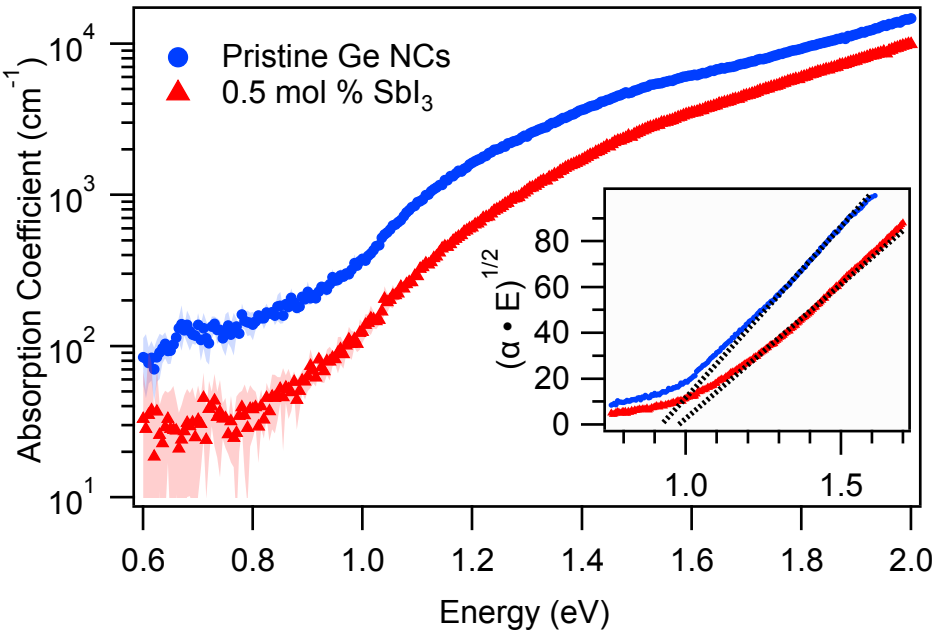

Figure 13. Absorption coefficient of pristine (blue circles) and 0.5 mol % Sb-doped (red triangles) Ge NCs, with error shown as the solid shading above and below each curve (most noticeable from 0.6 – 1.0 eV). The inset shows the indirect Tauc plot for each with the band gap fit shown as a dotted black line.

Electrical Characterization of Electron- and Hole-Only Devices. Current density - voltage (J-V) measurements for electron-only devices (EODs) and hole-only devices (HODs) of OAm/TOP-capped pristine and 0.5 mol % Sb-doped Ge NCs were taken to determine the conduction behavior upon the incorporation of Sb into the nanocrystals. Conductance for the devices can be found in Figure 14; J-V curves with the conductivity fits can be found in Figure S16. In both the pristine and Sb-doped electron-only devices, electron conduction is evident, though conduction in the Sb-doped device is reduced from the pristine NCs. Hole conduction from pristine to Sb-doped shows a significant change, going from purely resistive to conductive, within range of its electron-only counterpart. While we cannot comment on the nature of the pristine NCs (the energy of NC

valence states compared with the work functions of PEDOT:PSS/Au may create too great of an energy difference to allow any conduction), it is clear that the addition of Sb in the NCs increases hole conduction, contrary to what we would expect from the inclusion of an *n*-type dopant. This inclusion of Sb into Ge NCs, with a change in conduction, stands in contrast to the alloyed form achieved by Ruddy *et al.*[23]

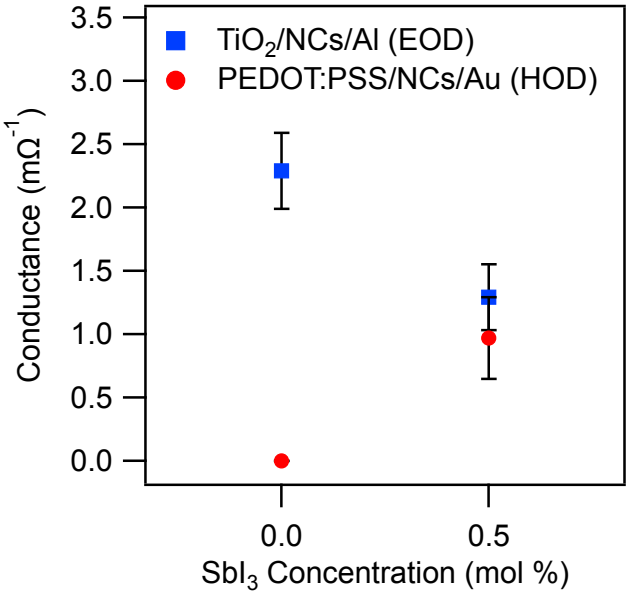

Figure 14. Conductance of electron-only devices (EODs, blue squares) and hole-only devices (HODs, red circles) as a function of Sb concentration.

EXAFS shows that at 0.5 mol % doping the majority of the Sb atoms reside within the particle and not at the surface, indicating the increase in hole conduction does not derive from defect states generated by Sb at the surface. Antimony-vacancy defects (Sb-V complex or E-centers) in germanium are well studied and the conversion of bulk Ge from *n*- to *p*-type has been observed after Sb-V defect generation by electron- or gamma-irradiation.[56–60] EXAFS supports the existence of these defects; this, combined with the increase in hole conduction, lead us to suspect that the

inclusion of Sb as a typical *n*-type dopant has instead resulted in *p*-type doping of the Ge NCs. However, further studies must be done to confirm this hypothesis, in addition to determining the charge state of the Sb-V defects and the transport properties of these materials.

Conclusions

Sb as a dopant has been successfully incorporated into colloidal Ge NCs. OAm and OAm/TOP were used as passivating ligands with OAm/TOP surface functionality resulting in consistently larger NCs. The coordination of TOP in combination with OAm on the Ge NC surface was confirmed by ^{1}H and ^{31}P NMR spectroscopy. SEM-EDS measurements confirm the presence of Sb in OAm-, OAm/TOP- and DDT-capped Sb-doped Ge NCs samples. XPS analysis performed on DDT-capped Ge NCs using 1.0 and 2.0 mol % SbI_3 confirms the presence of Sb after hydrazine treatment and OAm ligand removal suggesting a strong Sb interaction with Ge surface *versus* a labile physisorption of Sb atoms on Ge. EXAFS confirms the incorporation of Sb in the OAm- and OAm/TOP capped NCs, both within the core and on the surfaces of the crystallite grains. EXAFS analysis suggests a structural model with a mixed percentage of Sb dopants on surface sites and within the crystal in the form of Sb-vacancy pairs. The modeling of the data shows that as the Sb concentration and NC size increases, the fraction of Sb dopants on surface sites also increases. PDS confirms high levels of disorder in both pristine and 0.5 mol % Sb-doped Ge NCs. Electrical characterization indicates that the inclusion of Sb in the Ge NCs increases hole conduction. This, combined with previous studies, suggests that Sb-vacancy defects may generate *p*-type behavior in doped NCs, contrary to the expected *n*-type behavior by doping with Sb. The role Sb-vacancy defects play in transport in Ge NCs deserves further study.

Methods/Experimental

All syntheses and post-synthesis manipulations were conducted in an inert environment.

Germanium (II) iodide, GeI_2, was purchased from Prof. Richard Blair's laboratory (University of Central Florida) and shown to be phase pure by PXRD.[30,61] Antimony (III) iodide, SbI_3, (98%, Sigma-Aldrich) was used as received. Oleylamine, OAm, ((z)-Octadec-9-enylamine, $CH_3(CH_2)_7CH=CH-(CH_2)_7CH_2NH_2$, technical grade, >50%, TCI America) was degassed under vacuum for at least 2 h at 150 °C prior to use. 1-Dodecanethiol, DDT, (98%, Sigma-Aldrich) was degassed under vacuum at 150 °C for a minimum of 2 h prior to use. Hydrazine (anhydrous, 98%, Sigma-Aldrich) was used as received. Tri-n-octylphosphine, TOP, (97%, Sigma-Aldrich) was used as received. Methanol, toluene, hexane and acetonitrile (HPLC grade, Fisher Scientific) were purified using a solvent purification system and stored in a glove box under argon. Sodium sulfide, Na_2S (Sigma-Aldrich), was used as received. Formamide ($HCONH_2$, ≥ 99.5%, Sigma-Aldrich) was degassed under vacuum at 150 °C for a minimum of 2 h prior to use.

All syntheses of pristine and Sb-doped Ge NCs were carried out using a CEM microwave reactor (Discover SP) in dynamic mode. In a typical synthesis to prepare Ge NCs capped with either OAm or OAm/TOP on the surface, a 35 mL borosilicate microwave tube (from CEM) was loaded with 0.40 mmol (130.6 mg) of GeI_2 and 24.3 mmol (8.0 mL) degassed OAm or OAm/TOP (OAm/TOP ratio of 7:1 v/v) was added using a calibrated pipet in an argon-filled glovebox. The microwave reaction vessel was sealed with a Teflon cap (from CEM). The tube was sonicated in a water bath at room temperature for 10 min until complete dissolution of GeI_2 to form a pale-yellow solution. The contents of the microwave tube were heated to 250 ºC for 60 min in the microwave reactor. The color of the final solution was dark brown. To isolate the Ge NCs, the microwave tube containing the final product was transferred to an argon-filled glovebox. The contents of the microwave tube were transferred to a 50 mL centrifuge tube and 2-3 mL of

anhydrous toluene or hexane and anhydrous methanol or ethanol as an anti-solvent (to the point of solution turbidity) were added. The solution was centrifuged at 8500 rpm (10016 rcf) at room temperature for 15 min, then the centrifuge tube was transferred to the glovebox and the pale yellow to colorless supernatant was discarded and the dark-brown precipitate collected at the bottom of centrifuge tube was redispersed in 3-4 mL of toluene. The dispersion/ precipitation cycle was carried out two to three times to ensure the removal of all unbounded OAm and TOP ligands. The final toluene solution was kept in the argon-filled glovebox for further use and characterization.

To ensure that SbI_3 could be reduced by OAm, 0.40 mmol of Sb precursor (235.9 mg of SbI_3) was mixed with 8.0 mL of OAm, sonicated, and heated for 60 min at 250 ºC in the CEM microwave reactor. The product was isolated as described above. The phase-pure powder X-ray diffraction (PXRD) pattern of Sb with rhombohedral symmetry (space group $R\bar{3}m$ type A7, arsenic structure)[62] is provided in the Figure S17.

To facilitate the handling and improve the precision and the reproducibility, a stock solution of 0.04 M SbI_3 in OAm was freshly prepared by dissolving 0.200 mmol of SbI_3 (100.5 mg) in 5.0 mL of OAm. At the same time, 0.40 mmol (130.6 mg) of GeI_2 was loaded into a 35 mL microwave vessel in an argon-filled glovebox. Using a calibrated pipet, calculated volumes of SbI_3 stock solution were added to the GeI_2 solution in OAm or OAm/TOP, so that the total volume of the mixture (OAm/TOP) was 8.0 mL. The volumes added from the Sb stock solution were 50 µL (0.50 mol %), 100 µL (1.0 mol %), 150 µL (1.5 mol %) and 200 µL (2.0 mol %). The synthesis and isolation procedures were carried out as described above.

The surfaces of the as-synthesized Ge and Sb-doped Ge NCs are passivated with OAm or OAm/TOP ligands. To remove the ligands from the surface of Ge NCs 5.0 mL of 5 M hydrazine

solution, freshly made by mixing 0.80 mL of anhydrous hydrazine in 4.2 mL dry acetonitrile, was added to a 5.0 mL toluene dispersion of OAm or OAm/TOP-capped Ge or Sb-doped Ge NCs. The suspension was stirred at room temperature overnight under an inert atmosphere. The ligand-free Ge NCs were precipitated by centrifugation at 8500 rpm (10016 rcf) for 30 min at room temperature using 6.0 mL toluene. In addition, the precipitate was washed multiple times with 8.0 mL of acetonitrile to remove residual hydrazine, followed by multiple cycles of washing with hexane prior to final centrifugation. The lack of any stable suspension of the dark-brown precipitate in toluene or hexane qualitatively demonstrated the successful removal of organic ligands from the surface. The ligand-free Ge NCs were subsequently capped with DDT by the following procedure. To the dark-brown precipitate, 10.0 mL of DDT was added to the dark-brown precipitate and heated for 60 min at 150 ºC in the microwave reactor. The complete dispersion of Ge NCs in DDT was a qualitative indication of coordination of thiol ligands to the Ge NC surface. To isolate DDT-capped Ge NCs, 10.0 mL of toluene (or hexane) along with 20.0 mL of anti-solvent (methanol) were added to the reaction mixture, and after centrifugation at 8500 rpm (10016 rcf), the dark-brown DDT-capped Ge NCs (pristine or Sb-doped) were obtained. The precipitate was washed several times with hexane to remove all unassociated DDT. The final toluene dispersion of Ge NCs was stored in the glovebox for further characterization. The DDT-capped Ge NCs can also be stored under ambient conditions for several months without loss of dispersity.

Sufficient precaution should be considered while handling hydrazine due to its toxicity and low flashpoint at 52°C.

Powder X-ray Diffraction (PXRD) patterns were obtained using samples by drop-casting a toluene dispersion of 0.40 mL (~2 mg) Ge NCs onto a quartz substrate or silicon (Si_{510}) single-crystal zero-background holder. The dark brown film obtained after solvent evaporation was

scanned using Bruker D8 Advance diffractometer (Cu-Kα, 40 kV, 40 mA, λ=1.5418 Å) in a 2θ range of 20°-80° with a 0.02º/step size and a 4 second exposure or on a Rigaku Miniflex 600 diffractometer dTex (Cu-Kα, λ = 1.5418 Å). Scans for Rietveld refinement were collected from 20°-80° with a 0.02º/step size and a 4 second exposure. The obtained patterns were compared to diamond cubic Ge (04-0545) powder diffraction file from the International Center of Diffraction Data (ICDD) database. Rietveld refinements were performed on OAm-capped Ge NCs with ~10 wt. % Si as a lattice parameter standard to obtain the lattice parameter using the JANA 2006 package.[63] To estimate the crystallite size, the Scherrer equation was employed, fitting the 220 reflection (Pseudo-Voigt) using Jade 6.0 software.[38,64]

Electron-transparent specimens for both transmission electron microscopy (TEM) and scanning transmission electron microscopy (STEM) were prepared by drop-casting dilute dispersions of Ge NCs in toluene onto either a holey carbon film supported by a 300 mesh copper specimen grid (SPI), or lacy carbon coated 400 mesh copper grid (Ted Pella). The grids were oven dried overnight at 80 °C to minimize any contamination during electron beam irradiation. The transmission electron microscopy imaging of the samples was performed using a JEOL-JEM 2500SE transmission electron microscope (JEOL Ltd. Tokyo, Japan) operated at 200 keV, and equipped with a Schottky field-emission electron gun (FEG) and a retractable 1k × 1k Gatan Multiscan CCD camera (model 794). Digital Micrograph software provided by Gatan Inc. was used to capture images. To determine the average particle size and respective standard deviation, 100-250 individual NCs were imaged from different areas on the grids. Particle sizes were determined using the ImageJ software package.[65] Some NCs were also imaged at 200 keV in STEM mode with an aberration-corrected JEOL JEM-2100F/Cs STEM equipped with a Gatan annular dark field (ADF) detector. For STEM imaging, the electron probe convergence semi-angle

was approximately 23 mrad and the ADF inner detector semi-angle was 33 mrad, resulting in medium angle annular dark field contrast for which some diffraction contrast cannot be neglected. Scanning electron microscopy (SEM) imaging and Energy Dispersive Spectroscopy (EDS) were carried out on a FEI Scios Dual Beam SEM at an acceleration voltage of 20 kV. The samples were prepared by drop-casting concentrated Sb-doped Ge NC solution in toluene onto a 1×1 cm^2 silicon substrate, followed by drying at room temperature under vacuum overnight. EDS mapping of the samples was conducted using Oxford Aztec EDS software.

Attenuated total reflectance-Fourier transform Infrared Spectroscopy, ATR-FTIR measurements were carried out on a Bruker Alpha spectrophotometer in transmittance or absorbance modes on samples prepared by drop-drying the NCs suspensions on the instrument's ATR chip.

Samples for ^{1}H and ^{31}P Nuclear Magnetic Resonance (NMR) Spectroscopy were prepared by evaporating toluene dispersions of Ge NCs in a vacuum oven at 80 °C and dissolving them in deuterated chloroform ($CDCl_3$) or deuterated benzene-d_6 (C_6D_6) solvents in argon-filled glovebox. NMR spectra were obtained at room temperature on a 400 MHz Bruker Avance IIIHD Nanobay Spectrometer or 600 MHz Varian VNMR spectrometer. Chemical shifts in the ^{1}H NMR spectra were referenced to residual undeuterated $CHCl_3$ (7.24 ppm) or undeuterated C_6H_6 (7.26 ppm).

X-ray Photoelectron Spectroscopy Apectroscopy (XPS) on DDT-capped pristine and Sb-doped Ge NCs was carried out using a Kratos Axis Ultra X-ray photoelectron spectrometer with an analyzer lens in hybrid mode. High-resolution scans were collected using a monochromatic aluminum anode with an operating current of 6 mA and voltage of 10 kV using a step size of 0.1 eV, a pass energy of 40 eV, and a pressure range of $1–4 \times 10^{-8}$ Torr. The binding energies for all spectra were referenced to the C 1*s* core level at 284.8 eV. Samples were prepared by drop-casting

dispersions of Ge NCs onto cleaned Cu substrates under anaerobic conditions followed by drying at 90 °C.

Extended X-ray absorption fine structure (EXAFS) measurements were conducted on pristine and Sb-doped Ge NCs that were characterized as described above. In a nitrogen-filled glovebox, Ge NC dispersions in toluene were drop-cast onto a 3 × 12 mm^2 piece of filter paper. Then, the solvent was evaporated at room temperature. The process was repeated multiple times to achieve even coverage of the NCs on the filter paper and to deposit sufficient material to achieve a desirable step height at the Ge K edge (0.5). To prevent oxidation, the prepared samples were sealed in 3M® 600 Transparent Scotch Tape, which is transparent to X-rays.

EXAFS measurements were performed on beam line 4-1 at the Stanford Synchrotron Radiation Lightsource (SSRL). For spectra collection, samples were held in an Oxford helium cryostat to maintain temperatures below 10 K. The X-ray beam was passed through a Si 220 double crystal monochromator ($\varphi = 0$), which was detuned 70% at 11.250 keV and 30.600 KeV for the Ge and Sb edge measurements, respectively. The Ge K edge occurs at 11.100 keV. Ge K edge spectra were collected in transmission mode with nitrogen gas used in the I_0 (incident), I_t (transmitted), and reference detectors. An energy resolution of 1.9 eV was obtained for the Ge K edge spectra using a 0.4 mm vertical slit. The Sb K edge occurs at 30.491 KeV. Sb K edge spectra were collected in fluorescence mode. The samples were placed at a 45° angle to the X-ray beam, and a 30 channel Ge detector was used. Argon gas was used in the I_0, I_t, and reference detectors. An energy resolution of 6.3 eV was obtained for the Sb K edge spectra using a 0.2 mm vertical slit. Spectra were collected for bulk Ge and Sb powders as references, and the spectra reported at both edges for each Ge NC sample are an average of three to four scans.

Standard procedures in the R-Space X-ray Absorption Package (RSXAP) were used to reduce the EXAFS data.[66] For the Sb K edge, glitches were removed; this was not required for the Ge K edge data. Then, the pre- and post-edge backgrounds were subtracted, and the step-height was normalized. The EXAFS k-space oscillations were extracted and then Fast Fourier transformed (FFT) into real space (r-space). FT ranges of 3.5-14.5 $Å^{-1}$ and 4.0-12.0 $Å^{-1}$ were used for the Ge and Sb K edges, respectively. Both FT windows were Gaussian rounded by 0.2 $Å^{-1}$. Examples of the k-space oscillations for both edges are given in Figure S18. The r-space spectra were fit to a sum of theoretical functions that were calculated for a Ge diamond cubic crystal structure using the FEFF7 code.[55] Fits included the first three Ge neighbors around a central Ge and Sb atoms. The distances to various neighbors were allowed to vary. The fitted amplitude of the pair distribution function for a pair of neighbors is given by $N*S_o^2$, where N is the number of neighbors and S_o^2 is the amplitude reduction factor. S_o^2 is very close to 1.0 for bulk Ge; also S_o^2 was set to 1.0 for the Sb edge data based on earlier studies.[67] The width, σ, of the pair distribution function is correlated to the amplitude; this correlation contributes to absolute uncertainties of 10-20% for N and σ^2.

Transverse photothermal deflection spectroscopy (PDS) was performed on thin films of OAm/TOP-capped pristine and 0.5 mol% Sb-doped Ge NCs. Films of each were prepared by depositing 40 μL of solution on a borosilicate glass slide and spinning at 400 RPM. Films were then dried at 50 °C for 5 minutes. Slides were cleaned with alconox and DI water, sonicated in acetone and isopropanol for 15 minutes, and dried with N_2 prior to deposition. The slides were then inserted into Fluorinert FC-72 (3M) and sampled under monochromatic light from 0.6 eV to 3.0 eV, at a step of 0.005 eV. Approximate band gaps were determined by plotting the Tauc relation $(\alpha \cdot E)^{1/n}\ vs.\ E$, where $n = 2$ for indirect transitions. Urbach energy, a characterization of

the collective disorder in the system, was found by fitting to the relation $\alpha \sim \exp\left(\frac{h\nu}{E_U}\right)$ in the mid-gap region. Sample preparation and loading was conducted in a dry, nitrogen filled glovebox and characterization occurred in a sealed holder to prevent oxidation during probing.

The PDS monochromatic pump beam is provided by a dual housing Oriel light source with a tungsten halogen lamp, passing through FELH400, FELH0700, FELH1000, and FELH 1500 longpass filters (Thorlabs) to an Acton SpectraPro monochromator with entry and exit slits at 10 mm and 3 mm respectively. The light is focused on the sample suspended and sealed in FC-72 Fluorinert within a quartz cuvette. The pump beam is modulated at 5 Hz by a Thorlabs filter wheel and the sample is probed with a 2 mW He-Ne laser beam (JDSU). As the sample heats and cools due to non-radiative relaxation from the excitation of the pump beam, the probe, which is focused at and runs parallel to the sample, deflects in the transparent, highly temperature sensitive liquid. These deflections are measured by a position sensitive detector (Thorlabs) and registered in a lock-in amplifier. In addition, the pump beam intensity is measured with a pyroelectric photo detector (Gentec). The voltages from the lock-ins are converted to absorption coefficient by $\alpha = \frac{-1}{d}\ln\left(1 - \frac{V_{sig}}{V_{ref}} C_{norm}\right)$, where $\boldsymbol{\alpha}$ is the absorption coefficient, d is the thickness of the film, V_{sig} is the voltage generated from the probe beam, V_{ref} is the voltage generated from the pump beam, and C_{norm} is a scaling constant determined by transmission at high absorbance from UV-Vis spectroscopy. These measurements allow sensitive detection of absorption, without influence from reflection or scattering, from 1-10^5 cm^{-1}.

Thin film electron-only devices (EODs) and hole-only devices (HODs) were fabricated to understand the electrical behavior of the pristine and Sb-doped Ge NCs. To reduce the influence of a built-in potential across the NC layer, devices were constructed with nearly aligned energy

levels of the electron/hole injection layer and the metallic contact. EODs consist of a titanium dioxide (TiO_2, Solaronix) electron injection layer (4.1 eV) with an aluminum electron injecting metal contact (4.0-4.2 eV); HODs were made with a hole injection layer of high conductivity grade poly(3,4-ethylenedioxythiophene) poly(styrenesulfonate) (PEDOT:PSS, Sigma-Aldrich, 5.1-5.2 eV) with a gold hole injecting metal contact (5.1-5.2 eV).

Both device architectures were deposited onto indium tin-oxide (ITO) patterned Eagle XG glass slides (Thin Film Devices). Slides were cleaned with alconox and deionized water, sonicated in acetone and isopropyl alcohol, then dried with nitrogen. For the EODs, a TiO_2 dense blocking layer was deposited *via* screen printing and placed on a hotplate at 115 ℃ for 5 minutes before sintering at 500 ℃ for 45 minutes. After sintering, a mesoporous TiO_2 layer was fabricated in the same way. For HODs, 40 uL PEDOT:PSS was spun at 3000 RPM for 60 seconds, then dried under vacuum at 125 ℃. Pristine and 0.5 mol % Sb doped Ge NCs capped with OAm/TOP were spun at 400 rpm using 40 uL for 45 seconds, with an additional 25 uL deposited drop-wise in the first 10 seconds to increase thickness to 150 nm ± 15 nm. The Ge NC films were dried at 50 ℃ for 5 minutes. Finally, aluminum or gold was thermally evaporated forming 100 nm metallic contacts. Architectures for both the EODs and HODs can be seen in Figure 15. Current-voltage measurements were performed under dark conditions on each device from -1.0 V to 1.0 V with a Keithly 2400 multimeter. All fabrication and characterization beginning with the deposition of the Ge NCs was performed in a dry nitrogen-filled glove box.

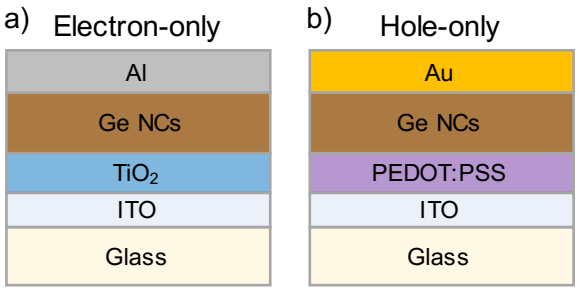

Figure 15. Thin film architectures for a) electron-only devices (EODs) and b) hole-only devices (HODs). TiO_2 serves as an electron injection layer in the EOD with aluminum as the top contact and at a similar energy level. PEDOT:PSS serves as a hole-injection layer in the HOD, with matching energy levels to the top contact of gold.

Acknowledgement

We acknowledge Dr. Elayaraja Muthuswamy for useful discussions and Phoenix N. H. Gllagher and Shayan Zargar for assistance with initial device fabrication. This work was supported by the National Science Foundation CHE-1710110. H.L., R.L.B and the XPS data collection were supported by the National Science Foundation DMR-1904719. The authors thank the Advanced Materials and Characterization Laboratory and the Center for Nano-MicroManufacturing at UC Davis for access to the TEM and SEM-EDS, respectively. The EXAFS experiments were performed at the Stanford Synchrotron Radiation Lightsource (SSRL), which is supported by the U.S. Department of Energy, Office of Science, Office of Basic Energy Sciences under Contract No. DE-AC02-76SF00515.

Supporting Information

Rietveld refined PXRD of OAm-capped Ge NC samples, TEM size distributions, PXRD of OAm/TOP- and DDT-capped Sb-doped Ge NCs, Bright field TEM, FTIR transmission spectra, ^{31}P NMR, SEM and EDS, XPS, and J-V Curves, PXRD of Sb, k-space plots for Ge and Sb K edge EXAFS data; Tables of Ge-Ge K Edge EXAFS Nearest Neighbors and values of some σ^2 for the Ge and Sb edges.

References

(1) Holman, Z. C.; Liu, C. Y.; Kortshagen, U. R. Germanium and Silicon Nanocrystal Thin-Film Field-Effect Transistors from Solution. *Nano Lett.* **2010**, *10* (7), 2661–2666. https://doi.org/10.1021/nl101413d.

(2) Carolan, D. Recent Advances in Germanium Nanocrystals: Synthesis, Optical Properties and Applications. *Prog. Mater. Sci.* **2017**, *90*, 128–158. https://doi.org/10.1016/j.pmatsci.2017.07.005.

(3) Vörös, M.; Wippermann, S.; Somogyi, B.; Gali, A.; Rocca, D.; Galli, G.; Zimanyi, G. T. Germanium Nanoparticles with Non-Diamond Core Structures for Solar Energy Conversion. *J. Mater. Chem. A* **2014**, *2* (25), 9820–9827. https://doi.org/10.1039/c4ta01543f.

(4) Ruddy, D. A.; Johnson, J. C.; Smith, E. R.; Neale, N. R. Size and Bandgap Control in the Solution-Phase Synthesis of Near-Infrared-Emitting Germanium Nanocrystals. *ACS Nano* **2010**, *4* (12), 7459–7466. https://doi.org/10.1021/nn102728u.

(5) Pillarisetty, R. Academic and Industry Research Progress in Germanium Nanodevices. *Nature*. **2011**, *479* (1-2), 324–328. https://doi.org/10.1038/nature10678.

(6) Maeda, Y.; Tsukamoto, N.; Yazawa, Y.; Kanemitsu, Y.; Masumoto, Y. Visible Photoluminescence of Ge Microcrystals Embedded in SiO_2 Glassy Matrices. *Appl. Phys. Lett.* **1991**, *59* (24), 3168–3170. https://doi.org/10.1063/1.105773.

(7) Xue, D. J.; Wang, J. J.; Wang, Y. Q.; Xin, S.; Guo, Y. G.; Wan, L. J. Facile Synthesis of Germanium Nanocrystals and Their Application in Organic-Inorganic Hybrid Photodetectors. *Adv. Mater.* **2011**, *23* (32), 3704–3707. https://doi.org/10.1002/adma.201101436.

(8) Ramasamy, K.; Kotula, P. G.; Fidler, A. F.; Brumbach, M. T.; Pietryga, J. M.; Ivanov, S. A. Sn_xGe_{1-x} Alloy Nanocrystals: A First Step toward Solution-Processed Group IV Photovoltaics. *Chem. Mater.* **2015**, *27* (13), 4640–4649. https://doi.org/10.1021/acs.chemmater.5b01041.

(9) Chan, C. K.; Zhang, X. F.; Cui, Y. High Capacity Li Ion Battery Anodes Using Ge Nanowires. *Nano Lett.* **2008**, *8* (1), 307–309. https://doi.org/10.1021/nl0727157.

(10) Kamata, Y. High-k/Ge MOSFETs for Future Nanoelectronics. *Materials Today*. **2008**, *11*,

30–38. https://doi.org/10.1016/S1369-7021(07)70350-4.

(11) Seino, M.; Henderson, E. J.; Puzzo, D. P.; Kadota, N.; Ozin, G. A. Germanium Nanocrystal Doped Inverse Crystalline Silicon Opal. *J. Mater. Chem.* **2011**, *21* (40), 15895–15898. https://doi.org/10.1039/c1jm13172a.

(12) Vaughn, D. D.; Schaak, R. E. Synthesis, Properties and Applications of Colloidal Germanium and Germanium-Based Nanomaterials. *Chemical Society Reviews*. **2013**, *42*, 2861–2879. https://doi.org/10.1039/c2cs35364d.

(13) Fan, J.; Chu, P. K. Group IV Nanoparticles: Synthesis, Properties, and Biological Applications. *Small* **2010**, *6* (19), 2080–2098. https://doi.org/10.1002/smll.201000543.

(14) Gaponenko, S. V.; Gaponenko, S. V. *Semiconductor Nanocrystals (Quantum Dots)*; Springer: Wien, New York, London, **2012**. https://doi.org/10.1017/cbo9780511750502.006.

(15) Chikan, V. Challenges and Prospects of Electronic Doping of Colloidal Quantum Dots: Case Study of CdSe. *J. Phys. Chem. Lett.* **2011**, *2* (21), 2783–2789. https://doi.org/10.1021/jz2012325.

(16) Buonsanti, R.; Milliron, D. J. Chemistry of Doped Colloidal Nanocrystals. *Chem. Mater.* **2013**, *25* (8), 1305–1317. https://doi.org/10.1021/cm304104m.

(17) Chen, D.; Viswanatha, R.; Ong, G. L.; Xie, R.; Balasubramaninan, M.; Peng, X. Temperature Dependence of "Elementary Processes" in Doping Semiconductor Nanocrystals. *J. Am. Chem. Soc.* **2009**, *131* (26), 9333–9339. https://doi.org/10.1021/ja9018644.

(18) Sahu, A.; Kang, M. S.; Kompch, A.; Notthoff, C.; Wills, A. W.; Deng, D.; Winterer, M.; Frisbie, C. D.; Norris, D. J. Electronic Impurity Doping in CdSe Nanocrystals. *Nano Lett.* **2012**, *12* (5), 2587–2594. https://doi.org/10.1021/nl300880g.

(19) Engel, J. H.; Alivisatos, A. P. Postsynthetic Doping Control of Nanocrystal Thin Films: Balancing Space Charge to Improve Photovoltaic Efficiency. *Chem. Mater.* **2014**, *26* (1), 153–162. https://doi.org/10.1021/cm402383r.

(20) Yu, B.; Zebarjadi, M.; Wang, H.; Lukas, K.; Wang, H.; Wang, D.; Opeil, C.; Dresselhaus, M.; Chen, G.; Ren, Z. Enhancement of Thermoelectric Properties by Modulation-Doping in Silicon Germanium Alloy Nanocomposites. *Nano Lett.* **2012**, *12* (4), 2077–2082. https://doi.org/10.1021/nl3003045.

(21) Noone, K. M.; Ginger, D. S. Doping for Speed: Colloidal Nanoparticles for Thin-Film Optoelectronics. *ACS Nano* **2009**, *3* (2), 261–265. https://doi.org/10.1021/nn9000935.

(22) Zhang, H.; Pokhrel, S.; Ji, Z.; Meng, H.; Wang, X.; Lin, S.; Chang, C. H.; Li, L.; Li, R.; Sun, B.; Wang, M.; Liao, Y. P.; Liu, R.; Xia, T.; Madler, L.; Nel, A. E. PdO Doping Tunes Band-Gap Energy Levels as Well as Oxidative Stress Responses to a Co_3O_4 *p*-Type Semiconductor in Cells and the Lung. *J. Am. Chem. Soc.* **2014**, *136* (17), 6406–6420. https://doi.org/10.1021/ja501699e.

(23) Ruddy, D. A.; Erslev, P. T.; Habas, S. E.; Seabold, J. A.; Neale, N. R. Surface Chemistry

Exchange of Alloyed Germanium Nanocrystals: A Pathway toward Conductive Group IV Nanocrystal Films. *J. Phys. Chem. Lett.* **2013**, *4* (3), 416–421. https://doi.org/10.1021/jz3020875.

(24) Barth, S.; Seifner, M. S.; Maldonado, S. Metastable Group IV Allotropes and Solid Solutions: Nanoparticles and Nanowires. *Chem. Mater.* **2020**, *32* (7), 2703–2741. https://doi.org/10.1021/acs.chemmater.9b04471.

(25) Chen, P. C.; Liu, G.; Zhou, Y.; Brown, K. A.; Chernyak, N.; Hedrick, J. L.; He, S.; Xie, Z.; Lin, Q. Y.; Dravid, V. P.; O'Neill-Slawecki, S. A.; Mirkin, C. A. Tip-Directed Synthesis of Multimetallic Nanoparticles. *J. Am. Chem. Soc.* **2015**, *137* (28), 9167–9173. https://doi.org/10.1021/jacs.5b05139.

(26) Chen, P.-C.; Liu, X.; Hedrick, J. L.; Xie, Z.; Wang, S.; Lin, Q.-Y.; Hersam, M. C.; Dravid, V. P.; Mirkin, C. A. Polyelemental Nanoparticle Libraries. *Science.* **2016**, *352* (6293), 1565–1569.

(27) Bi (Bismuth) Binary Alloy Phase Diagrams, Ge-Bi (Online) *Alloy Phase Diagrams,* Vol 3, *ASM Handbook*, Edited by Okamoto, H.; Schlesinger, M. E.; Mueller, E. M. ASM International, **2016**, p 201-217. https://doi.rg/10.31399/asm.hb.v03.a0006150.

(28) Esteves, R. J. A.; Ho, M. Q.; Arachchige, I. U. Nanocrystalline Group IV Alloy Semiconductors: Synthesis and Characterization of $Ge_{1-x}Sn_x$ Quantum Dots for Tunable Bandgaps. *Chem. Mater.* **2015**, *27* (5), 1559–1568. https://doi.org/10.1021/cm503983b.

(29) Alguno, A.; Usami, N.; Ujihara, T.; Fujiwara, K.; Sazaki, G.; Nakajima, K.; Shiraki, Y. Enhanced Quantum Efficiency of Solar Cells with Self-Assembled Ge Dots Stacked in Multilayer Structure. *Appl. Phys. Lett.* **2003**, *83* (6), 1258–1260. https://doi.org/10.1063/1.1600838.

(30) Tabatabaei, K.; Lu, H.; Nolan, B. M.; Cen, X.; McCold, C. E.; Zhang, X.; Brutchey, R. L.; Van Benthem, K.; Hihath, J.; Kauzlarich, S. M. Bismuth Doping of Germanium Nanocrystals through Colloidal Chemistry. *Chem. Mater.* **2017**, *29* (17), 7353–7363. https://doi.org/10.1021/acs.chemmater.7b02241.

(31) Sully, H. R.; Tabatabaei, K.; Hellier, K.; Newton, K. A.; Ju, Z.; Knudson, L.; Zargar, S.; Wang, M.; Kauzlarich, S. M.; Bridges, F.; Carter, S. A. Characterizing Bismuth Doping of Colloidal Germanium Quantum Dots for Energy Conversion Applications. *ACS Appl. Nano Mater.* **2020**, *3* (6), 5410–5420. https://doi.org/10.1021/acsanm.0c00709.

(32) Lu, X.; Ziegler, K. J.; Ghezelbash, A.; Johnston, K. P.; Korgel, B. A. Synthesis of Germanium Nanocrystals in High Temperature Supercritical Fluid Solvents. *Nano Lett.* **2004**, *4* (5), 969–974. https://doi.org/10.1021/nl049831j.

(33) Henderson, E. J.; Hessel, C. M.; Veinot, J. G. C. Synthesis and Photoluminescent Properties of Size-Controlled Germanium Nanocrystals from Phenyl Trichlorogermane-Derived Polymers. *J. Am. Chem. Soc.* **2008**, *130* (11), 3624–3632. https://doi.org/10.1021/ja710286a.

(34) Muthuswamy, E.; Iskandar, A. S.; Amador, M. M.; Kauzlarich, S. M. Facile Synthesis of Germanium Nanoparticles with Size Control: Microwave *versus* Conventional Heating.

Chem. Mater. **2013**, *25* (8), 1416–1422. https://doi.org/10.1021/cm302229b.

(35) Muthuswamy, E.; Zhao, J.; Tabatabaei, K.; Amador, M. M.; Holmes, M. A.; Osterloh, F. E.; Kauzlarich, S. M. Thiol-Capped Germanium Nanocrystals: Preparation and Evidence for Quantum Size Effects. *Chem. Mater.* **2014**, *26* (6), 2138–2146. https://doi.org/10.1021/cm4042154.

(36) Chen, M.; Feng, Y. G.; Wang, X.; Li, T. C.; Zhang, J. Y.; Qian, D. J. Silver Nanoparticles Capped by Oleylamine: Formation, Growth, and Self-Organization. *Langmuir* **2007**, *23* (10), 5296–5304. https://doi.org/10.1021/la700553d.

(37) Xu, Z.; Shen, C.; Hou, Y.; Gao, H.; Sun, S. Oleylamine as Both Reducing Agent and Stabilizer in a Facile Synthesis of Magnetite Nanoparticles. *Chem. Mater.* **2009**, *21* (9), 1778–1780. https://doi.org/10.1021/cm802978z.

(38) Mourdikoudis, S.; Liz-Marzán, L. M. Oleylamine in Nanoparticle Synthesis. *Chem. Mater.* **2013**, *25* (9), 1465–1476. https://doi.org/10.1021/cm4000476.

(39) Barry, S. D.; Yang, Z.; Kelly, J. A.; Henderson, E. J.; Veinot, J. G. C. Synthesis of Si_xGe_{1-x} Nanocrystals Using Hydrogen Silsesquioxane and Soluble Germanium Diiodide Complexes. *Chem. Mater.* **2011**, *23* (22), 5096–5103. https://doi.org/10.1021/cm202761k.

(40) He, M.; Protesescu, L.; Caputo, R.; Krumeich, F.; Kovalenko, M. V. A General Synthesis Strategy for Monodisperse Metallic and Metalloid Nanoparticles (In, Ga, Bi, Sb, Zn, Cu, Sn, and Their Alloys) *via in Situ* Formed Metal Long-Chain Amides. *Chem. Mater.* **2015**, *27* (2), 635–647. https://doi.org/10.1021/cm5045144.

(41) Tabatabaei, K.; Holmes, A. L.; Newton, K. A.; Muthuswamy, E.; Sfadia, R.; Carter, S. A.; Kauzlarich, S. M. Halogen-Induced Crystallinity and Size Tuning of Microwave Synthesized Germanium Nanocrystals. *Chem. Mater.* **2019**, *31* (18), 7510–7521. https://doi.org/10.1021/acs.chemmater.9b02225.

(42) He, M.; Walter, M.; Kravchyk, K. V.; Erni, R.; Widmer, R.; Kovalenko, M. V. Monodisperse SnSb Nanocrystals for Li-Ion and Na-Ion Battery Anodes: Synergy and Dissonance between Sn and Sb. *Nanoscale* **2015**, *7* (2), 455–459. https://doi.org/10.1039/c4nr05604c.

(43) Walter, M.; Doswald, S.; Kovalenko, M. V. Inexpensive Colloidal SnSb Nanoalloys as Efficient Anode Materials for Lithium- and Sodium-Ion Batteries. *J. Mater. Chem. A* **2016**, *4* (18), 7053–7059. https://doi.org/10.1039/c5ta10568d.

(44) Xu, C.; Senaratne, C. L.; Kouvetakis, J.; Menéndez, J. Experimental Doping Dependence of the Lattice Parameter in *n* -Type Ge: Identifying the Correct Theoretical Framework by Comparison with Si. *Phys. Rev. B* **2016**, *93* (4), 041201–041205. https://doi.org/10.1103/PhysRevB.93.041201.

(45) Tuinenga, C.; Jasinski, J.; Iwamoto, T.; Chikan, V. *In Situ* Observation of Heterogeneous Growth of CdSe Quantum Dots: Effect of Indium Doping on the Growth Kinetics. *ACS Nano* **2008**, *2* (7), 1411–1421. https://doi.org/10.1021/nn700377q.

(46) Sun, Y.; Xia, Y. Shape-Controlled Synthesis of Gold and Silver Nanoparticles. *Science* **2002**, *298* (5601), 2176–2179. https://doi.org/10.1126/science.1077229.

(47) Talapin, D. V.; Rogach, A. L.; Mekis, I.; Haubold, S.; Kornowski, A.; Haase, M.; Weller, H. Synthesis and Surface Modification of Amino-Stabilized CdSe, CdTe and InP Nanocrystals. *Colloids Surfaces A: Physicochem. Eng. Asp.* **2002**, *202* (2–3), 145–154. https://doi.org/10.1016/S0927-7757(01)01078-0.

(48) Boles, M. A.; Ling, D.; Hyeon, T.; Talapin, D. V. Erratum: The Surface Science of Nanocrystals (Nature Materials (2016) 15 (141-153)). *Nat. Mater.* **2016**, *15* (3), 364. https://doi.org/10.1038/nmat4578.

(49) Caldwell, M. A.; Raoux, S.; Wang, R. Y.; Philip Wong, H. S.; Milliron, D. J. Synthesis and Size-Dependent Crystallization of Colloidal Germanium Telluride Nanoparticles. *J. Mater. Chem.* **2010**, *20* (7), 1285–1291. https://doi.org/10.1039/b917024c.

(50) Abel, K. A.; Shan, J.; Boyer, J.; Harris, F.; Veggel, F. C. J. M. Van. Highly Photoluminescent PbS Nanocrystals - The Beneficial Effect of Trioctylphosphine. *Chem. Mater.* **2008**, *20* (11), 3794–3796. https://doi.org/10.1021/cm702564a

(51) Newton, K. A.; Ju, Z.; Tabatabaei, K.; Kauzlarich, S. M. Diorganyl Dichalcogenides as Surface Capping Ligands for Germanium Nanocrystals. *Organometallic* **2020,** *39*, 995-1005 https://doi.org/10.1021/acs.organomet.9b00749.

(52) Smock, S. R.; Tabatabaei, K.; Williams, T. J.; Kauzlarich, S. M.; Brutchey, R. L. Surface Coordination Chemistry of Germanium Nanocrystals Synthesized by Microwave-Assisted Reduction in Oleylamine. *Nanoscale* **2020**, *12* (4), 2764–2772. https://doi.org/10.1039/c9nr09233a.

(53) Hens, Z.; Martins, J. C. A Solution NMR Toolbox for Characterizing the Surface Chemistry of Colloidal Nanocrystals. *Chem. Mater.* **2013**, *25* (8), 1211–1221. https://doi.org/10.1021/cm303361s.

(54) Thomson, J. W.; Nagashima, K.; MacDonald, P. M.; Ozin, G. A. From Sulfur-Amine Solutions to Metal Sulfide Nanocrystals: Peering into the Oleylamine-Sulfur Black Box. *J. Am. Chem. Soc.* **2011**, *133* (13), 5036–5041. https://doi.org/10.1021/ja1109997.

(55) Ankudinov, A.; Rehr, J. Relativistic Calculations of Spin-Dependent X-Ray Absorption Spectra. Phys. Rev. B - Condens. Matter Mater. Phys. **1997**, *56* (4), R1712–R1716. https://doi.org/10.1103/PhysRevB.56.R1712.

(56) Markevich, V. P.; Peaker, A. R.; Litvinov, V. V.; Emtsev, V. V.; Murin, L. I. Electronic Properties of Antimony-Vacancy Complex in Ge Crystals. *J. Appl. Phys.* **2004**, *95* (8), 4078–4083. https://doi.org/10.1063/1.1669059.

(57) Markevich, V. P.; Hawkins, I. D.; Peaker, A. R.; Emtsev, K. V.; Emtsev, V. V.; Litvinov, V. V.; Murin, L. I.; Dobaczewski, L. Vacancy-Group-V-Impurity Atom Pairs in Ge Crystals Doped with P, As, Sb, and Bi. *Phys. Rev. B - Condens. Matter Mater. Phys.* **2004**, *70* (23), 1–7. https://doi.org/10.1103/PhysRevB.70.235213.

(58) Patel, N. S.; Monmeyran, C.; Agarwal, A.; Kimerling, L. C. Point Defect States in Sb-Doped Germanium. *J. Appl. Phys.* **2015**, *118* (15). https://doi.org/10.1063/1.4933384.

(59) Lindberg, C. E.; Hansen, J. L.; Bomholt, P.; Mesli, A.; Nielsen, K. B.; Larsen, A. N.; Dobaczewski, L. The Antimony-Vacancy Defect in *p*-Type Germanium. *Appl. Phys. Lett.*

2005, *87* (17), 1–3. https://doi.org/10.1063/1.2112168.

(60) Barnard, A. W.; Auret, F. D.; Meyer, W. E. Annealing of the Sb-Vacancy and a Closely Related Radiation Induced Defect in *n*-Type Germanium. *Phys. B Condens. Matter* **2018**, *535*, 242–244. https://doi.org/10.1016/j.physb.2017.07.049.

(61) Restrepo, D. T.; Lynch, K. E.; Giesler, K.; Kuebler, S. M.; Blair, R. G. Low-Temperature (210 °C) Deposition of Crystalline Germanium *via in Situ* Disproportionation of GeI_2. *Mater. Res. Bull.* **2012**, *47* (11), 3484–3488. https://doi.org/10.1016/j.materresbull.2012.06.072.

(62) Buerger, M. *The Structures of the Elements*; Wiley-Interscience: New York, 1975; Vol. 19. https://doi.org/10.1016/0025-5416(75)90120-2.

(63) Petrícek, V.; Dušek, M.; Palatinus, L. Crystallographic Computing System JANA2006: General Features. *Zeitschrift fur Krist.* **2014**, *229* (5), 345–352. https://doi.org/10.1515/zkri-2014-1737.

(64) P, S. Bestimmung Der Größe Und Der Inneren Struktur von Kolloidteilchen Mittels Röntgenstrahlen. *Nachrichten von der Gesellschaft der Wissenschaften zu Göttingen, Math. Klasse* **1918**, *2*, 98–100.

(65) Schneider, C. A.; Rasband, W. S.; Eliceiri, K. W. NIH Image to ImageJ: 25 Years of Image Analysis. *Nat. Methods* **2012**, *9* (7), 671–675. https://doi.org/10.1038/nmeth.2089.

(66) Booth, C. H. *R-Space X-Ray Absorption Package*; Lawrence National Laboratory, Berkeley, CA, **2010**.

(67) Li, G. G.; Bridges, F.; Booth, C. H. X-Ray Absorption Fine-Structure Standards: A Comparison of Experiment and Theory. *Phys. Rev. B - Condens. Matter Mater. Phys.* **1995**, *52* (9), 6332-6348. https://doi.org/10.1103/PhysRevB.

TOC Figure